

Static Model-Based Optimization and Multi-Input Optimal Control of Automatic Transmission Upshift during Inertia Phase

Cvok, Ivan; Deur, Joško; Hihlik, Mislav; Zhang, Yijing; Ivanovic, Vladimir; Fujii, Yuji

Source / Izvornik: **Vehicles**, 2023, 5, 177 - 202

Journal article, Published version

Rad u časopisu, Objavljena verzija rada (izdavačev PDF)

<https://doi.org/10.3390/vehicles5010011>

Permanent link / Trajna poveznica: <https://um.nsk.hr/um:nbn:hr:235:939322>

Rights / Prava: [Attribution 4.0 International](#)/[Imenovanje 4.0 međunarodna](#)

Download date / Datum preuzimanja: **2025-01-07**

Repository / Repozitorij:

[Repository of Faculty of Mechanical Engineering
and Naval Architecture University of Zagreb](#)



Article

Static Model-Based Optimization and Multi-Input Optimal Control of Automatic Transmission Upshift during Inertia Phase

Ivan Cvok ^{1,*}, Joško Deur ¹, Mislav Hihlik ^{1,†}, Yijing Zhang ², Vladimir Ivanovic ² and Yuji Fujii ²

¹ Faculty of Mechanical Engineering and Naval Architecture, University of Zagreb, Ivana Lučića 5, HR-10002 Zagreb, Croatia

² Ford Motor Company—Research and Innovation Center, 2101 Village Rd, Dearborn, MI 48124, USA

* Correspondence: ivan.cvok@fsb.hr

† Dr. I. Cvok and Mr. M. Hihlik are currently with Rimac Technology d.o.o.

Abstract: Step-ratio automatic transmission upshift performance can be improved by modulating the off-going (OFG) clutch during the inertia phase. In this paper, a static powertrain performance model is derived and applied for the purpose of numerically efficient, multi-objective shift control parameter optimization for the inertia phase. The optimization is aimed at finding the optimal node parameters for simplified, piecewise linear, open-loop profiles of oncoming (ONC) clutch, OFG clutch, and engine torque reduction control variables. The performance indices, i.e., the optimization objectives, include shift comfort, clutch thermal loss, and shift time. The optimization results in 3D Pareto optimal frontiers, which are then analyzed and compared with those obtained by using the previously developed, nonlinear model-based, genetic algorithm optimization tool. The derived method is employed in order to develop a static model-based predictive control (S-MPC) strategy, which commands ONC clutch torque control input while retaining open-loop controls for engine and OFG clutch control inputs. The S-MPC strategy aims at providing the prespecified shift time, while the shift time accuracy is relaxed to some extent by using a control input dead zone element to avoid chattering effect. The S-MPC system performance is verified through simulation and compared with the genetic algorithm benchmark. The simulation results demonstrate that the S-MPC strategy approaches the benchmark performance.

Keywords: automotive systems; automatic transmission; shift control; optimization; optimal control; analysis



Citation: Cvok, I.; Deur, J.; Hihlik, M.; Zhang, Y.; Ivanovic, V.; Fujii, Y. Static Model-Based Optimization and Multi-Input Optimal Control of Automatic Transmission Upshift during Inertia Phase. *Vehicles* **2023**, *5*, 177–202. <https://doi.org/10.3390/vehicles5010011>

Academic Editor:
Stephan Rinderknecht

Received: 2 January 2023
Revised: 27 January 2023
Accepted: 3 February 2023
Published: 7 February 2023



Copyright: © 2023 by the authors. Licensee MDPI, Basel, Switzerland. This article is an open access article distributed under the terms and conditions of the Creative Commons Attribution (CC BY) license (<https://creativecommons.org/licenses/by/4.0/>).

1. Introduction

Step-ratio automatic transmissions (AT), equipped with torque converter, planetary gear sets, and wet clutches/brakes, are commonly found in conventional but also electrified powertrains [1,2]. A large number of AT gears (up to 10 for passenger vehicles, nowadays) introduces new types of shifts, such as multi-step and double-transition shifts, which are more difficult to control [2,3]. This places increased requirements on gear shift control system in terms of improving shift responsiveness, comfort, and energy efficiency [3].

Current AT shift control systems predominantly rely upon open-loop-generated control input profiles, whose parameters can effectively be determined by using off-line control parameter optimization (CPO) methods previously applied to conventional single-transition shifts [4,5] and more demanding double-transition shifts [6,7]. The control input profiles themselves can be designed based on the insights gained through control trajectory optimization (CTO), as presented in References [8,9] based on the examples of single- and double-transition shifts, respectively. Although CPO is faster and more straightforward than CTO, it still requires significant computational time to find optimal parameters, which motivates the development of new, simplified optimization approaches.

The emphasis of AT upshift controller design is usually on the inertia phase, where the main, oncoming (ONC) clutch torque control action is supplemented by the engine torque reduction action implemented through a fuel cut or spark retardation control channel [1] in order to reduce the uncomfortable output shaft torque overshoot. Since open-loop shift control is rarely robust to AT parameter variations, it is usually supplemented by closed-loop control actions aimed at tracking the desired ONC clutch slip speed or engine speed reference to ensure shift duration [1]. Different formulations of closed-loop control systems are proposed in the literature, such as PID control [10], robust control [11], and LPV control [12]. The drawback of these methods is that the ONC clutch control action does not directly account for (and anticipate) the open-loop engine control action. For better overall performance, more advanced, multi-input/multi-output (MIMO) closed-loop control strategies can be applied, which are typically based on linear quadratic regulators (LQR) [13–15] and model predictive controllers (MPC) [16,17]. Although the advanced MIMO methods offer performance improvements over open-loop and basic closed-loop control strategies, they may be computationally demanding and require full-state feedback that may not be available in application.

During the upshift inertia phase, the ONC clutch and engine torque control inputs may be augmented by the off-going (OFG) clutch torque input. The benefit of using OFG clutch during the inertia phase, i.e., introducing a controlled tie-up of the two clutches, is the suppression of output shaft torque oscillation and/or the prevention of the engine flair at the inertia phase start, as confirmed by bond-graph analysis in Reference [18] and experimentally in Reference [19]. It is demonstrated through CTO in Reference [8] and CPO in Reference [20] that using the OFG clutch either reduces shift time or improves shift comfort at the expense of somewhat increased clutch energy loss. LQR-based MIMO control involving the OFG clutch during the inertia phase is considered in References [14,15].

This paper expands on the work presented in Reference [20] by proposing a simplified control parameter optimization approach for the upshift inertia phase based on an analytical, static model of shift objectives. This approach is further employed in order to formulate a practical, static model-based model predictive control (S-MPC) law. The S-MPC law utilizes the ONC clutch slip speed feedback signal and commands the ONC clutch torque capacity based on the static model prediction of the open-loop engine and OFG clutch control actions. This constitutes the following main contributions of the paper: (i) a numerically efficient shift control parameter optimization method based on analytical static model of optimization objectives and (ii) a corresponding, simple-to-implement, computationally inexpensive, and robust model predictive control strategy.

The remainder of this paper is organized as follows. Section 2 describes a control-oriented powertrain dynamics model including a 10-speed AT submodel. Section 3 overviews the genetic algorithm-based control parameter optimization results for 1–3 upshift based on Reference [20]. The static model-based optimization method is presented in Section 4, while the corresponding simulation analysis results are given in Section 5. The S-MPC strategy is proposed and verified in Section 6. Concluding remarks are given in Section 7.

2. Powertrain Dynamics Model

The mechanical scheme of the considered powertrain and the corresponding control-oriented bond graph are shown in Figure 1 [21,22]. A source-of-torque element is used to model the spark ignition engine, where the dependence of torque τ_e on the accelerator pedal position p_{th} and the engine speed ω_e is established through an experimentally recorded engine map. The engine rotational dynamics are described by:

$$I_{ei}\dot{\omega}_e = (\tau_e(p_{th}, \omega_e) - \Delta\tau_{ec}) - \tau_i, \quad (1)$$

where I_{ei} is the total, engine and impeller moment of inertia, $\Delta\tau_{ec}$ denotes the engine torque cutting control input, and τ_i is the impeller torque.

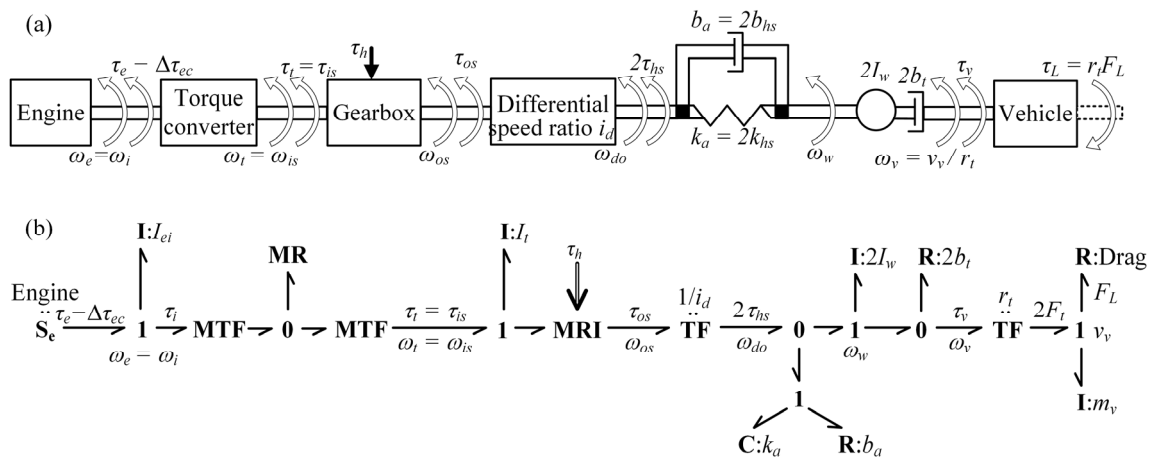


Figure 1. Powertrain schematic (a) and corresponding control-oriented bond-graph model (b).

The torque converter is represented by nonlinear static maps $R_\tau(R_\omega)$ and $K_i(R_\omega)$, where $R_\omega = \omega_t/\omega_i = \omega_t/\omega_e$ is the speed ratio, and $R_\tau = \tau_t/\tau_i$ and $K_i = \omega_i/\sqrt{\tau_i}$ are the torque ratio and the capacity factor, respectively. This gives the following torque converter static model (see Reference [22] and references therein):

$$\tau_i = \frac{\omega_e^2}{K_i^2(R_\omega)}, \tag{2a}$$

$$\tau_t = R_\tau(R_\omega)\tau_i. \tag{2b}$$

The considered 10-speed AT gearbox [23] includes four planetary gear sets, four clutches, and two brakes. A full, sixth-order mathematical model of the considered 10-speed AT [23] gearbox is derived in References [24,25]. When accounting for locked and open clutch/brake states for a given single-transition shift, the following reduced-order model can be obtained, which is represented by the bond graph shown in Figure 2 [25,26]:

$$\underbrace{\begin{bmatrix} I_{in} & I_{io} \\ I_{io} & I_{out} \end{bmatrix}}_{\mathbf{A}_{red}} \begin{bmatrix} \dot{\omega}_{is} \\ \dot{\omega}_{os} \end{bmatrix} = \underbrace{\begin{bmatrix} 1 & 0 & -i_1 & -i_2 \\ 0 & -1 & g_1^{-1} & g_2^{-1} \end{bmatrix}}_{\mathbf{B}_{red}} \begin{bmatrix} \tau_{is} \\ \tau_{os} \\ \tau_{OFG} \\ \tau_{ONC} \end{bmatrix}, \tag{3a}$$

$$\underbrace{\begin{bmatrix} \omega_{OFG} \\ \omega_{ONC} \end{bmatrix}}_{\mathbf{U}_{red}} = \underbrace{\begin{bmatrix} i_1 & -g_1^{-1} \\ i_2 & -g_2^{-1} \end{bmatrix}}_{\mathbf{U}_{red}} \begin{bmatrix} \omega_{is} \\ \omega_{os} \end{bmatrix}, \tag{3b}$$

where the gearbox input speed $\omega_{is} = \omega_t$ and the output speed ω_{os} constitutes the state vector, while the off-going (OFG) clutch torque τ_{OFG} , the oncoming (ONC) clutch torque τ_{ONC} , the gearbox input torque $\tau_{is} = \tau_t$ and the output torque τ_{os} form the input vector. The inertia matrix \mathbf{A}_{red} contains equivalent gearbox input and output inertia I_{in} and I_{out} , respectively, as well as the cross-coupling inertia I_{io} . The input matrix \mathbf{B}_{red} contains the equivalent input/output gear ratios i_1, g_1 and i_2, g_2 of the OFG and ONC clutch torque transfer paths (Figure 2). It should be mentioned that the bond graph in Figure 2 is applicable to another common type of AT, which is dual clutch transmission (DCT), with the main being difference that there is no inertia coupling effect (nor the torque converter in Figure 1a). Thus, the optimization and control methods proposed in this paper are applicable to DCTs, as well.

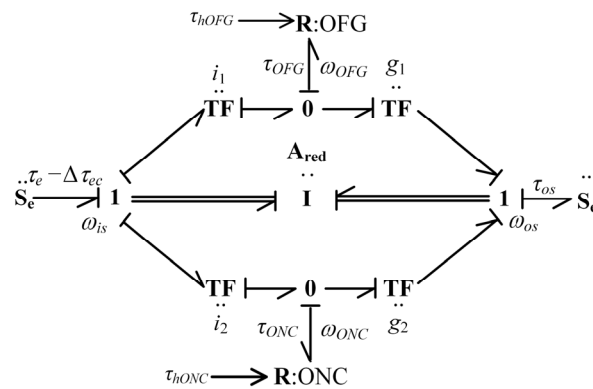


Figure 2. Bond graph model of AT gearbox dynamics for single-transition shifts.

The AT model further simplifies in the case of a locked torque converter, where $\omega_{is} = \omega_i = \omega_e$ and $\tau_{is} = \tau_i = \tau_e - \Delta\tau_{ec}$ hold. The engine rotational dynamics given by Equation (1) become redundant [25], and the engine-side inertia I_{ei} is lumped to the torque converter turbine inertia I_{in} given in the gearbox state Equation (3a).

A clutch friction model is used to determine the clutch torques $\tau_j, j \in \{OFG, ONC\}$, in Equation (3a) based on the clutch slip speeds ω_j given by Equation (3b). Here, the Karnopp friction model [27] is used, which is described as [22]:

$$\tau_j = \begin{cases} \tau_{f,slip}(\omega_j) = \tau_{hj}\bar{T}_C \text{sgn}(\omega_j), & \text{for } |\omega_j| \geq \Delta\omega \\ \tau_{f,stick} = \text{sat}(\tau_{stick,j}, \tau_{hj}\bar{T}_C), & \text{otherwise} \end{cases} \quad (4)$$

where τ_{hj} is the commanded clutch torque capacity, $\bar{T}_C = 1$ is the normalized Coulomb friction torque, and $\tau_{stick,j}$ is the locked clutch element hold torque that is obtained from slipping clutch and input/output torques [22]. The clutch actuator dynamics are not considered (except in a control system robustness test in Section 6) for the sake of simplicity and in order to establish benchmark performance in a straightforward manner.

The differential reduces the gearbox output speed ($\omega_{do} = \omega_{os}/i_d$) and provides equal left and right halfshaft torque $\tau_{hs} = i_d \tau_{os}/2$ (Figure 1). The halfshafts are modeled by an equivalent compliant shaft (Figure 1, [21,22]). Details on the driveline and longitudinal dynamics submodels are given in Reference [7]. Note that a linearized, adhesion-region tire model is used, and that the zero amount of road slope and a constant rolling resistance are assumed.

3. Control Parameter Optimization

The previously developed, genetic algorithm-based method/tool of AT shift control parameter multi-objective optimization (CPO) [5] is employed in order to provide a benchmark for the simplified optimization method and the control strategy proposed in this paper. The method optimizes the break point parameters of practical, piecewise-linear AT control input profiles based on the full, sixth-order, nonlinear powertrain dynamics model, as is elaborated upon in Reference [20].

3.1. Problem Formulation

The aim of optimization is to find the ONC and OFG clutch capacity and engine torque reduction profile parameters defined in Figure 3, which minimize the following shift objectives [20]:

$$\min_{\mathbf{P}_{ctrl}} J_1 = t_{shift}, \quad (5a)$$

$$\min_{\mathbf{P}_{ctrl}} J_2 = j_{RMS} = \sqrt{\frac{1}{t_f} \int_0^{t_f} \ddot{v}_v^2 dt}, \quad (5b)$$

$$\min_{\mathbf{p}_{ctrl}} J_3 = E_{loss} = \int_0^{t_f} \sum_j \omega_j \tau_j dt, j \in \{OFG, ONC\}, \tag{5c}$$

which relate to shift time, root-mean-square (RMS) vehicle jerk, and clutch energy loss, respectively, where the jerk j corresponds to the second derivative of vehicle velocity v_v denoted in Figure 1. The optimized control parameters contained in the vector \mathbf{p}_{ctrl} are denoted in Figure 3 by blue-box labels. The control parameters are subject to inequality constraints corresponding to their limit values, and the optimization is subject to additional constraints in order to prevent very short torque phase duration and shift time, as well as to provide zero ONC slip speed in the post-shift phase (see Reference [20] for more details).

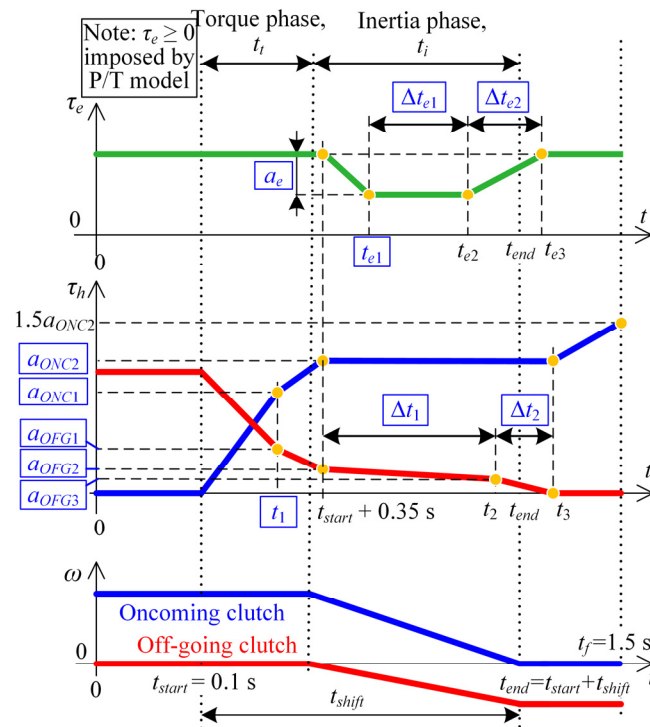


Figure 3. Definition of the upshift control profiles used in control parameter optimization (CPO).

The following four scenarios are considered, which define the number and type of control inputs/actuators used in the inertia phase:

1. ONC clutch only,
2. ONC and OFG clutch,
3. ONC clutch and engine torque reduction,
4. ONC and OFG clutch including engine torque reduction.

The shift operating conditions are defined as follows: (i) 1–3 shift is considered as one of the most demanding upshifts due to the high gear ratio step, (ii) both open and locked torque converter cases are taken into account, and (iii) the accelerator pedal opening is fixed to 30% ($p_{th} = 0.3$) with the initial engine speed set to $\omega_{e0} = 2500$ rpm.

Note that Figure 3 relates to Scenario 4, where all the three control inputs are used. In other scenarios, the unused control input(s) are simply omitted. For example, in Scenarios 1 and 3, the OFG clutch is not used, so $a_{OFG2,3}$ are set to 0, and Δt_1 and Δt_2 are not optimized. In all scenarios, shift is initiated at $t_{start} = 0.1$ s, and the final time is fixed at $t_f = 1.5$ s.

The optimization problem is solved by applying the multi-objective genetic algorithm MOGA-II incorporated within the modeFRONTIER optimization environment, which runs the powertrain dynamics model implemented in Matlab/Simulink [5,20]. In this study, 30 initial designs (generated as a Sobol sequence) and 200 population generations are used, which gives 6000 evaluations of the objectives given by Equation (5).

3.2. Optimization Results

The CPO-obtained Pareto optimal frontiers are shown in Figure 4a,b for the cases of open and locked torque converters, respectively. In both cases, introducing additional control inputs during the inertia phase, i.e., engine or OFG clutch torque inputs, moves the frontier towards the utopia point (0, 0, 0). Introducing the OFG clutch torque control input allows for shorter shift while retaining shift comfort (vertical move of a Pareto optimal point for Scenario 1 \rightarrow 2 and Scenario 3 \rightarrow 4; for example, from A to B in the latter case as shown in Figure 4a), or a more comfortable shift in the the same amount of shift time (horizontal move of a Pareto optimal point). Additionally, reducing the engine torque during the inertia phase (Scenario 1 \rightarrow 3 and Scenario 2 \rightarrow 4) results in cutting the clutches' energy loss, and at the same time allows for shorter or more comfortable shift. Unlike 2D Pareto frontiers belonging to Scenarios 1 and 3, 3D frontiers occur for Scenarios 2 and 4, thus indicating that all the three shift control criteria are conflicting in the OFG clutch application scenarios. While the general trends are the same in the cases of locked and open torque converters, it is worth noting that in the locked torque converter case the performance is worse as the frontiers are shifted towards higher RMS jerk values, mainly due to the lack of torque converter-related damping [20].

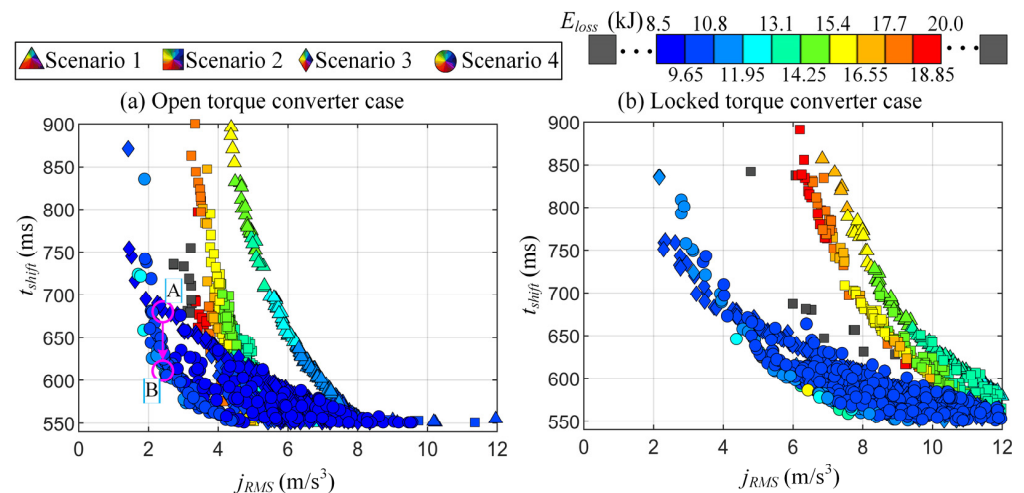


Figure 4. Comparative CPO results for different control scenarios in the case of open (a) and locked torque converters (b).

Figure 5 shows the comparative time responses that correspond to Pareto optimal Point A (Scenario 3; dashed line) and Point B (Scenario 4; solid line) denoted in Figure 4a. The OFG clutch hold torque is negative at the shift start, and it changes its sign once the ONC clutch becomes the primary torque carrier. As soon as the OFG clutch hold torque overcomes the OFG clutch torque capacity, the OFG clutch starts slipping, and the inertia phase begins. Introducing OFG clutch control during the inertia phase results in reducing the shift time by 9% and the inertia phase duration by 20% (see the dotted blue lines in Figure 5), while maintaining the RMS jerk at roughly the same level (Table 1). This requires a higher level of ONC clutch torque during the inertia phase (Figure 5c; [20]), which results in an increased total clutch power loss peak (Figure 5f) and the total clutch energy loss rises by 4% (Table 1). In both cases, the output shaft speed marginally increases during the inertia phase, while the engine and input shaft speeds decrease in a linear-like manner (see Figure 5b). This results in nearly linear fall of the ONC clutch slip speed.

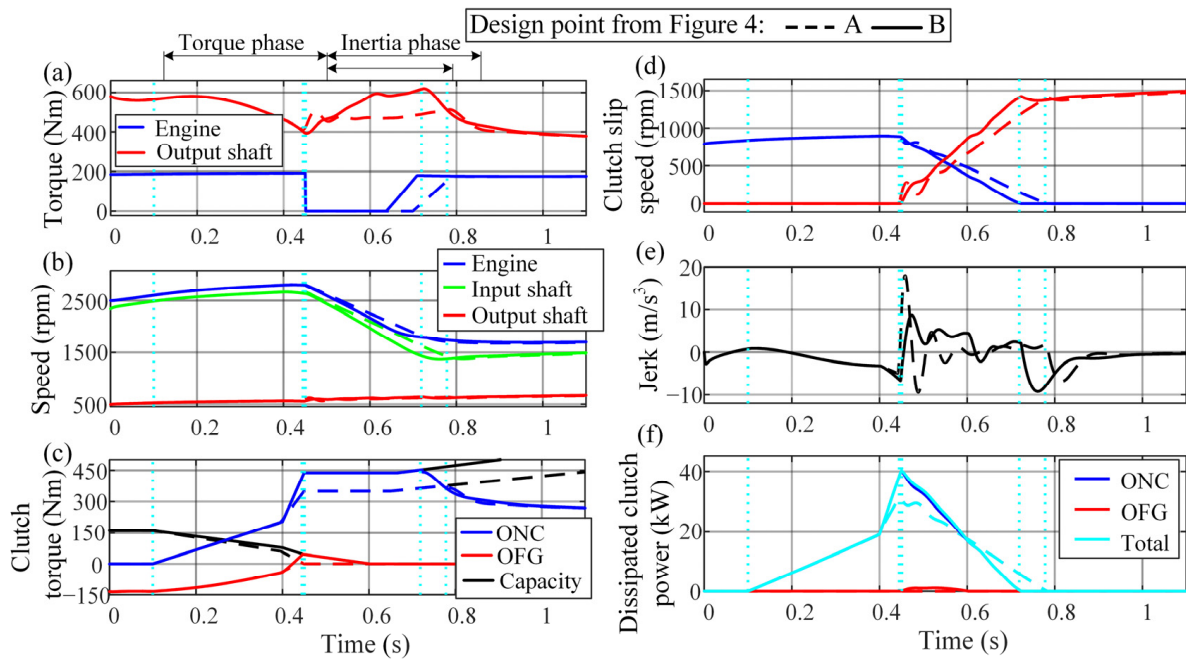


Figure 5. Time responses of torques (a), shaft speeds (b), clutch torques and speeds (c,d), jerk (e) and dissipated clutch power (f) of CPO designs for Scenario 3 (A) and Scenario 4 (B) in the open torque converter case.

Table 1. Comparative values of the performance indices corresponding to optimal responses are shown in Figure 5 and the design points are from Figure 4.

Point	j_{RMS} (m/s ³)	t_{shift} (ms)	E_{loss} (kJ)
A (Scenario 3)	2.64	678	9.4
B (Scenario 4)	2.68 (+1.5%)	619 (−8.7%)	9.76 (+3.8%)

4. Static Model-Based Optimization

The CPO method relied on a nonlinear powertrain dynamics simulation model to evaluate the optimization objectives (5). By introducing certain assumptions during the inertia phase based on the optimal automatic transmission behavior observed in Figure 5, it is possible to simplify the objective-calculation model into a static form, thus making the optimization computationally more efficient compared to CPO. A faster optimization method can potentially be employed online.

4.1. Model Simplification

In order to facilitate model simplification, certain assumptions are introduced, as described below and depicted in Figure 6. Based on the CPO results from Figure 5, the output shaft speed may be considered constant during the inertia phase due to large vehicle inertia and relatively short shift time:

$$\dot{\omega}_{os} = 0 \Rightarrow \omega_{os} = \text{const.}, \tag{6}$$

and it is further denoted as a constant parameter ω_{osir} , which is set to the output shaft speed value at the beginning of the inertia phase. Similarly, the base engine torque is assumed to be constant throughout the inertia phase ($\tau_e = \tau_{ei}$) and set to the engine torque at the beginning of the inertia phase. The assumption is justified by the relatively short upshift inertia phase, during which the accelerator pedal is not expected to change significantly and the variation of engine torque due to engine speed change is modest.

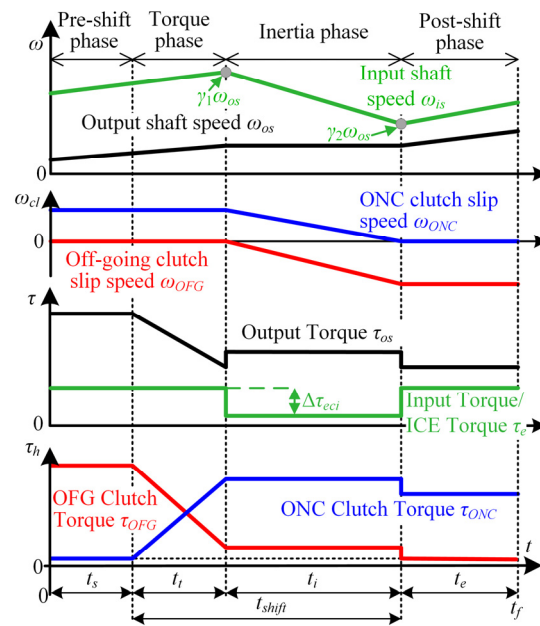


Figure 6. Simplified AT variable profiles based on assumptions of constant output shaft speed and constant control inputs during the inertia phase.

While accounting for assumption (6), the gearbox model (3a) can be rewritten as:

$$I_{in}\dot{\omega}_{is} = \tau_{is} - i_1\tau_{ofg} - i_2\tau_{onc}, \tag{7a}$$

$$\tau_{os} = -\frac{I_{io}}{I_{in}}\tau_{is} + \left(\frac{i_1 I_{io}}{I_{in}} + \frac{1}{g_1}\right)\tau_{ofg} + \left(\frac{i_2 I_{io}}{I_{in}} + \frac{1}{g_2}\right)\tau_{onc}. \tag{7b}$$

Combining Equations (1) and (2b) yields:

$$\tau_{is} = \tau_t = R_\tau(R_\omega)(\tau_{ei} - \Delta\tau_{ec} - I_{ei}\dot{\omega}_e) \tag{8}$$

According to the characteristic torque converter responses shown in Figure 7a and corresponding to the inertia phase of Figure 5, the speed ratio $R_\omega = \omega_t/\omega_i$ does not vary significantly during the inertia phase. Therefore, it may be assumed that the torque converter speed ratio R_ω and consequently the torque ratio $R_\tau(R_\omega)$ are constant during the inertia phase. Similarly, based on the responses shown in Figure 7b, one may assume that for (a majority of) inertia phase the torque converter acceleration ratio $R_{\dot{\omega}} = \dot{\omega}_{is}/\dot{\omega}_e = \dot{\omega}_t/\dot{\omega}_i$ is constant.

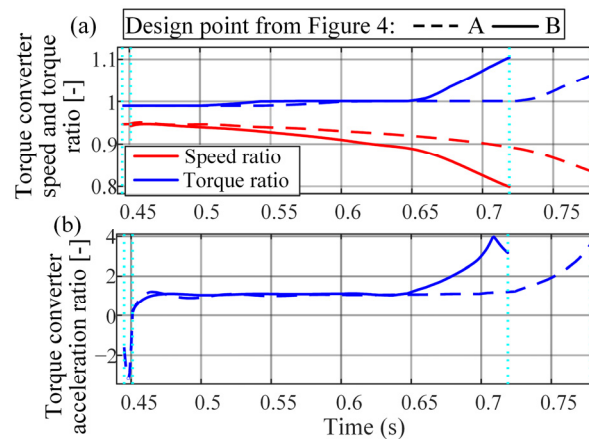


Figure 7. Response of torque converter torque and speed ratios (a) and acceleration ratio (b) during inertia phase corresponding to responses given in Figure 5.

By substituting the equation $\dot{\omega}_e = \dot{\omega}_{is}/R_{\dot{\omega}}$ into Equation (8) and inserting the resulting expression in Equation (7), the following simplified model is obtained in the open torque converter case:

$$I_{eq}\dot{\omega}_{is} = R_{\tau}(\tau_{ei} - \Delta\tau_{ec}) - i_1\tau_{OFG} - i_2\tau_{ONC}, \tag{9a}$$

$$\tau_{os} = k_{os,e}(\tau_{ei} - \Delta\tau_{ec}) + k_{os,OFG}\tau_{OFG} + k_{os,ONC}\tau_{ONC}, \tag{9b}$$

where the equivalent input shaft inertia I_{eq} and the newly introduced output shaft torque model coefficients read:

$$I_{eq} = I_{in} + I_{ei}\frac{R_{\tau}}{R_{\dot{\omega}}}, \quad \begin{aligned} k_{os,ONC} &= \frac{1}{g_2} + \frac{i_2 I_{io}}{I_{eq}}, \\ k_{os,OFG} &= \frac{1}{g_1} + \frac{i_1 I_{io}}{I_{eq}}, \\ k_{os,e} &= -\frac{I_{io} R_{\tau}}{I_{eq}}. \end{aligned} \tag{10}$$

The model corresponding to the locked torque converter case can readily be obtained from Equations (9) and (10) by inserting $R_{\dot{\omega}}=1$ and $R_{\tau}=1$.

The clutch torques τ_{OFG} and τ_{ONC} , and the engine torque reduction $\Delta\tau_{ec}$ can be profiled as piecewise linear functions (see Figure 5), or, for the sake of simplicity, they can be fixed to constant values during the inertia phase (Figure 6). Equation (9) indicates that in the latter case, the output shaft torque τ_{os} and the input shaft deceleration $\dot{\omega}_{is}$ are constant as well.

The constant values of torque converter ratios R_{τ} and $R_{\dot{\omega}}$ have been determined by averaging the CPO simulation time-responses throughout the inertia phase (see samples in Figure 7) and for all Pareto optimal designs of a single shift control scenario (see Figure 4). The obtained results are represented by minimum, maximum, and mean values given in Table 2. The mean values are further considered, whereas opting for minimum or maximum values was found to only slightly affect the obtained results.

Table 2. Statistics of the average torque converter torque and acceleration ratios during the inertia phase, related to the CPO-obtained Pareto optimal designs for different control scenarios.

Scenario	Min	R_{τ} Mean	Max	Min	$R_{\dot{\omega}}$ Mean	Max
1	1.00	1.03	1.05	1.14	1.48	1.64
2	1.00	1.03	1.05	1.22	1.51	1.81
3	1.00	1.00	1.02	1.09	1.34	1.61
4	1.00	1.01	1.02	1.11	1.26	1.61

4.2. Definition of Optimization Objectives

The aim is to define proper forms of shift objectives related to those given by Equation (5), which could be algebraically (statically) expressed in terms of clutch and engine torque control inputs to be optimized.

4.2.1. Inertia Phase Duration

The upshift inertia phase duration t_i can be derived by integrating the input shaft torque equilibrium Equation (9a) and taking into account the following initial and final conditions (see Figure 6):

$$\begin{aligned} \omega_{is}(0) &= \omega_{osi}\gamma_1, \\ \omega_{is}(t_i) &= \omega_{osi}\gamma_2, \end{aligned} \tag{11}$$

where

$$\gamma_1 = (i_1 g_1)^{-1} > \gamma_2 = (i_2 g_2)^{-1} > 0, \tag{12}$$

are the starting (lower; γ_1) and ending (higher; γ_2) gear ratios. This gives

$$(\gamma_1 - \gamma_2)\omega_{osi} = \frac{1}{I_{eq}} \int_0^{t_i} (i_2\tau_{ONC}(t) + i_1\tau_{OFG}(t) - R_\tau(\tau_{ei} - \Delta\tau_{ec}(t)))dt, \quad (13)$$

The final expression for the inertia phase duration t_i is obtained by solving the integral Equation (13) for specified profiles of the control inputs τ_{ONC} , τ_{OFG} , and $\Delta\tau_{ec}$ (see Section 4.3).

4.2.2. Energy Loss in Inertia Phase

The clutch energy loss during the inertia phase is defined by Equation (5c), with t_f being replaced by t_i . By using Equation (3b) and the constant $\omega_{os} = \omega_{osi}$ based on Equation (6), one obtains

$$E_i = \int_0^{t_i} \left(\tau_{ONC}(t) \left(i_2\omega_{is}(t) - g_2^{-1}\omega_{osi} \right) + \tau_{OFG}(t) \left(i_1\omega_{is}(t) - g_1^{-1}\omega_{osi} \right) \right) dt, \quad (14)$$

where ω_{is} is obtained by integrating Equation (9a):

$$\omega_{is}(t) = \frac{1}{I_{eq}} \int_0^t (R_\tau(\tau_{ei} - \Delta\tau_{ec}(t)) - i_2\tau_{ONC}(t) - i_1\tau_{OFG}(t))dt, \quad (15)$$

4.2.3. Shift Comfort Equivalent

The vehicle jerk cannot be expressed as a static function of control inputs. Therefore, an inertia bump level metric is introduced as an equivalent of the RMS jerk objective, and it is defined as the relative increase of mean output shaft torque ($\bar{\tau}_{os}$) with respect to the target gear output shaft torque $\gamma_2\tau_{is} = \gamma_2R_\tau\tau_e \approx \gamma_2\tau_{ei}$:

$$\rho_{ib} = \frac{\bar{\tau}_{os}}{\gamma_2\tau_{ei}} - 1, \quad (16)$$

where the mean output shaft torque is obtained by integrating Equation (9b):

$$\bar{\tau}_{os} = \frac{1}{t_i} \int_0^{t_i} (k_{os,e}(\tau_{ei} - \Delta\tau_{ec}(t)) + k_{os,OFG}\tau_{OFG}(t) + k_{os,ONC}\tau_{ONC}(t))dt, \quad (17)$$

4.3. Final Expressions for Optimization Objectives

The general expressions defined in Section 4.2 are applied to two specific control input formulations in order to derive final expressions to be used in the optimization of control input parameters. The first, simple formulation relies on the assumption of constant control inputs throughout the upshift inertia phase (see Figure 6). In the second formulation, the OFG clutch is described by a piecewise linear profile (see CPO setup and results given in Figures 3 and 5, respectively), while the ONC clutch torque and the engine torque reduction profiles are still assumed to be constant.

4.3.1. Constant Control Inputs

The presumably constant control inputs during the inertia phase (Figure 6) are denoted as τ_{ONCi} , τ_{OFGi} , and $\Delta\tau_{eci}$. In this case, Equation (13) has the following solution for inertia phase duration:

$$t_i = \frac{I_{eq}(\gamma_1 - \gamma_2)\omega_{osi}}{i_2\tau_{ONCi} + i_1\tau_{OFGi} - R_\tau(\tau_{ei} - \Delta\tau_{eci})}, \quad (18)$$

The total clutch energy loss is obtained by solving Equation (14) and accounting for Equation (18) and rearranging, which yields

$$E_i = (\gamma_1 - \gamma_2)\omega_{osi}\frac{t_i}{2}(i_2\tau_{ONCi} - i_1\tau_{OFGi}) = \frac{(\gamma_1 - \gamma_2)^2 I_{eq}\omega_{osi}^2}{2} \frac{i_2\tau_{ONCi} - i_1\tau_{OFGi}}{i_2\tau_{ONCi} + i_1\tau_{OFGi} - R_\tau(\tau_{ei} - \Delta\tau_{eci})} \quad (19)$$

Finally, the inertia bump index is obtained from Equations (16) and (17) as

$$\rho_{ib} = \frac{1}{\gamma_2} \frac{k_{os,e}(\tau_{ei} - \Delta\tau_{eci}) + k_{os,OFG}\tau_{OFGi} + k_{os,ONC}\tau_{ONCi}}{\tau_{ei}} - 1 \quad (20)$$

4.3.2. Piecewise Linear Profile of Off-Going Clutch Torque Control Input

By following the CPO formulation (Figure 3, [20]), the OFG clutch torque control input profile can be made piecewise linear for improved performance. According to Figure 8, the applied profile includes two break points, and it is defined by four parameters: τ_{OFG0} , τ_{OFG1} , t_1 , and t_2 . The other two control inputs are kept at the constant levels τ_{ONCi} and $\Delta\tau_{eci}$.

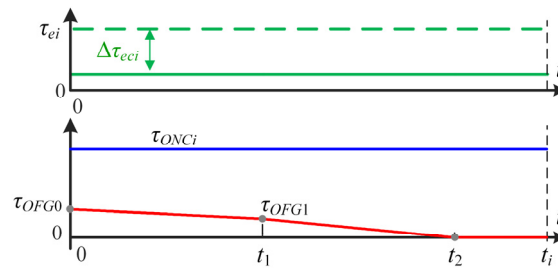


Figure 8. Definition of the piecewise linear profile of OFG clutch torque control input during the upshift inertia phase.

Solving Equation (13) for the control input profiles defined in Figure 8 gives the following final expression for inertia phase duration:

$$t_i = \frac{(\gamma_1 - \gamma_2)I_{eq}\omega_{osi} + \frac{i_1}{2}(\tau_{OFG0}t_1 + \tau_{OFG1}t_2)}{i_2\tau_{ONCi} - R_\tau(\tau_{ei} - \Delta\tau_{eci})} \quad (21)$$

Solving Equation (14) and rearranging yields the total clutch energy loss formula given in Appendix A as Equation (A1). Finally, based on Equations (16) and (17), the following final expression is obtained for the inertia bump index:

$$\rho_{ib} = \frac{k_{os,e}(\tau_{ei} - \Delta\tau_{eci}) + k_{os,ONC}\tau_{ONCi} + \frac{k_{os,OFG}(\tau_{OFG0}t_1 + \tau_{OFG1}t_2)(i_2\tau_{ONCi} - R_\tau(\tau_{ei} - \Delta\tau_{eci}))}{2(\gamma_1 - \gamma_2)I_{eq}\omega_{osi} + i_1(\tau_{OFG0}t_1 + \tau_{OFG1}t_2)}}{\gamma_2\tau_{ei}} - 1, \quad (22)$$

4.4. Optimization Framework

The optimization is aimed at finding the optimal control input parameters

$$\mathbf{p} = \begin{cases} \begin{bmatrix} \tau_{ONCi} & \tau_{OFGi} & \Delta\tau_{eci} \end{bmatrix}, & \text{for constant control inputs} \\ \begin{bmatrix} \tau_{ONCi} & \Delta\tau_{eci} & \tau_{OFG0} & \tau_{OFG1} & t_1 & t_2 \end{bmatrix}, & \text{for piecewise linear profile of } \tau_{OFG} \end{cases}$$

which minimize either the inertia phase duration t_i or the total clutch energy loss E_i , subject to equality constraint on inertia bump ratio and inequality constraints related to parameter bounds. Thus, the optimization problem is defined as

$$\mathbf{p} = \operatorname{argmin} t_i \text{ or,} \quad (23)$$

$$\begin{aligned}
 \mathbf{p} &= \operatorname{argmin} E_i, & (24) \\
 &\text{subject to :} \\
 \mathbf{P}_{\min} &\leq \mathbf{P} \leq \mathbf{P}_{\max}, \\
 \rho_{ib} &= \rho_{ibR}.
 \end{aligned}$$

The optimization objectives t_i and E_i , and the inertia bump constraint ρ_{ib} are defined by Equations (18)–(20) in the case of constant control inputs, and Equations (21), (22) and (35) in the case of the piecewise linear profile of τ_{OFG} . Note that in the latter case, the additional constraint $t_1 < t_2$ is applied to comply with the profile definition in Figure 8. The values of the control parameter limits \mathbf{p}_{\min} and \mathbf{p}_{\max} are given in Section 5.

Solving the minimum time and minimum energy loss optimization problems (23) and (24), respectively, for different levels of the inertia bump ratio targets ρ_{ibR} results in a pair of boundary 2D Pareto frontiers. They edge a 3D Pareto frontier, which would be a solution of the optimization problem concerning minimization of all the three objectives (t_i , E_i , and ρ_{ib}), and as such, it would reflect the CPO 3D Pareto frontiers shown in Figure 4.

The above formulation falls in the category of constrained nonlinear optimization problems. The problem is solved in MATLAB by using a sequential quadratic program (SQP) algorithm implemented through function *fmincon*.

4.5. Algebraic Analysis for Constant Control Input Case

An algebraic analysis is conducted in order to better understand the influence of OFG clutch torque modulation during the inertia phase on the shift performance and facilitate understanding of optimization results from Sections 3 and 5. In order to enable algebraic analysis, only the constant control input case is considered, and it is assumed that (i) the torque converter is locked ($R_\tau = 1$ and $R_\omega = 1$) and (ii) the inertia coupling is negligible ($I_{io} = 0$).

4.5.1. Inertia Phase Duration

By expressing the ONC clutch torque τ_{ONC} based on Equation (9b) and inserting it in Equation (18) as the constant control input τ_{ONCi} dependent on the constant output torque τ_{osi} , the inertia phase duration can be expressed as:

$$t_i = \frac{(\gamma_1 - \gamma_2)(I_{in} + I_{ei})\omega_{osi}}{-\tau_{ei} + \Delta\tau_{eci} + \frac{\tau_{osi}}{\gamma_2} - \frac{\gamma_1 - \gamma_2}{\gamma_1\gamma_2} \frac{\tau_{OFGi}}{g_1}}, \quad (25)$$

The following inequalities, related to the denominator terms of Equation (25), hold for an upshift:

$$\tau_{osi} > \gamma_2\tau_{ei} > \gamma_2(\tau_{ei} - \Delta\tau_{eci}), \quad (26a)$$

$$\frac{\tau_{OFGi}}{g_1} < 0, \quad (26b)$$

where Equation (26a) reflects the fact that the output shaft torque is greater during the inertia phase than in the new (higher) gear (i.e., the inertia bump occurs; see Figure 5), while Equation (26b) relates to the occurrence of OFG clutch power recirculation during the upshift inertia phase, as proven and discussed in Reference [20].

Based on Equation (25) and conditions (26) and (12), it is evident that increase of the OFG clutch torque τ_{OFGi} results in a decrease of the inertia phase duration t_i , i.e., in a faster shift. Similarly, the higher the engine torque reduction level $\Delta\tau_{eci} > 0$, the shorter is the inertia phase. Finally, increasing the output shaft torque target τ_{osi} , i.e., allowing for the higher inertia bump, results in a shorter inertia phase. These findings are in agreement with the CPO results given in Section 3 and the bond graph analysis results presented in Reference [20].

4.5.2. Total Clutch Energy Loss

Expressing the ONC clutch torque from Equation (18) and substituting it in Equation (19), together with $\tau_{OFGi} = 0$ (no OFG clutch control, Scenarios 1 and 3), yields the following expression for clutch energy loss

$$E_i = (\gamma_1 - \gamma_2)^2 \frac{(I_{in} + I_{ei})\omega_{osi}^2}{2} + (\gamma_1 - \gamma_2)(\tau_{ei} - \Delta\tau_{eci})\frac{\omega_{osi}}{2}t_i. \quad (27)$$

It follows from Equation (27) and Equation (12) that in Scenario 1, where $\Delta\tau_{eci} = 0$, the energy loss falls with the decrease in inertia phase duration t_i or base engine torque τ_{ei} . This means that the energy loss and inertia phase duration are not conflicting criteria, thus explaining the 2D form of the Pareto frontier observed in Figure 4 for Scenario 1. Additionally, Equation (27) points out that the engine torque reduction, applied in Scenario 3, decreases the energy loss and that in the case of full engine torque reduction ($\Delta\tau_{eci} = \tau_{ei}$), the energy loss does not depend on the inertia phase duration t_i .

For Scenarios 2 and 4 (OFG clutch control applied, $\tau_{OFGi} \neq 0$), after expressing the clutch torques $\tau_{ONC} = \tau_{ONCi}$ and $\tau_{OFG} = \tau_{OFGi}$ from the system of Equations (9b) and (18), inserting these torques in Equation (19), and rearranging, one obtains

$$E_i = (\gamma_1^2 - \gamma_2^2) \frac{(I_{in} + I_{ei})\omega_{osi}^2}{2} + (-2\tau_{osi} + (\tau_{ei} - \Delta\tau_{eci})(\gamma_1 + \gamma_2))\frac{\omega_{osi}}{2}t_i. \quad (28)$$

The first right-hand-side term of Equation (28) corresponds to the change in input kinetic energy, which is positive based on Equation (12). The second right-hand-side term of Equation (28) indicates that the energy loss is lower for shorter inertia phases (lower t_i), if the following condition is satisfied:

$$\tau_{ei} - \Delta\tau_{eci} > K\tau_{osi}, \quad (29)$$

with

$$K = \frac{2}{\gamma_1 + \gamma_2},$$

otherwise, the energy loss becomes higher for shorter inertia phases.

If no engine torque reduction is considered (Scenario 2, $\Delta\tau_{eci} = 0$), then the boundary output shaft torque $\tau_{os,l}$, above which the energy loss increases for shorter inertia phase, i.e., the condition (29) becomes invalid, equals $\tau_{os,l} = \tau_{ei}/K$. By inserting this equation into Equation (16) and accounting for the 1–3 upshift gear ratio values [20]: $\gamma_1 = 4.70$ and $\gamma_2 = 2.18 \Rightarrow K = 0.29$, one obtains the corresponding, lower-boundary inertia bump level:

$$\rho_{ib,l} = (K\gamma_2)^{-1} - 1 = \frac{1}{2} \left(\frac{\gamma_1}{\gamma_2} - 1 \right) = 0.58 = 58\%$$

The actual values of the inertia bump in Scenario 2 are typically higher than 58% for fast shifts due to the high gear ratio step $\gamma_1/\gamma_2 = 2.16$, and the condition (29) is rarely satisfied, thus meaning that the energy loss E_i typically increases with the shortening of the inertia phase duration t_i . In other words, E_i and t_i do represent conflicting criteria, and a 3D Pareto frontier is obtained for shorter shift times, as observed in Figure 4 for Scenario 2. On the other hand, the inertia bump would fall below 58% for a long inertia phase, thus leading to the reduction of the Pareto Frontier to 2D form in the region of slow shifts (Figure 4).

For Scenario 4 and the case of full engine torque reduction ($\Delta\tau_{eci} = \tau_{ei}$), which often occurs for energy efficiency reasons (Section 3), the left-hand side of condition (29) becomes zero. Therefore, condition (29) is never satisfied, and the energy loss is always higher for shorter inertia phases, thus giving the Pareto frontier a distinctive 3D form (Figure 4). The energy loss from Scenarios 2 and 4 is analyzed in more detail in Reference [28], including vehicle demonstration results that confirm the analysis.

5. Optimization Results and Performance Analysis

This section first presents the static model-based optimization results. The optimized control inputs are then applied within the control-oriented nonlinear simulation model from Section 2, and the obtained control performance is compared with the CPO benchmark results from Section 3.

5.1. Optimization Results

Static model-based optimization results are obtained by solving the minimum time and minimum energy loss optimization problems given by Equations (23) and (24), respectively. The optimizations are executed for inertia bump level targets ρ_{ibR} ranging from 0 to 2.5 in the steps of 0.05. The 1–3 upshift is considered, with the output shaft speed and the engine base torque set to $\omega_{osi} = 592$ rpm and $\tau_{ei} = 187$ Nm, respectively (Figure 5).

5.1.1. Constant Control Inputs

In the case of constant control input (Figure 6), optimization has been performed for both open and locked torque converter cases. The control parameter constraints are given in Table 3, and they are based on the limit values observed in CPO results (Figure 4; see e.g., Figure 5), in order to obtain realistic/feasible results in the simplified, static model-based optimization.

Table 3. Control parameter constraints for constant control input case.

Constraints		
0 Nm	$\leq \tau_{ONCi} \leq$	1000 Nm
20 Nm	$\leq \tau_{OFGi} \leq$	70 Nm
0 Nm	$\leq \Delta\tau_{eci} \leq$	τ_{ei}

The obtained Pareto frontiers are shown in Figure 9. In Scenario 1 (triangles) and Scenario 3 (diamonds), minimum-time (black line) and minimum-energy loss frontiers (red dashed line) coincide with each other. This confirms that in these scenarios the energy loss objective does not conflict with the inertia phase duration objective (cf. analysis results related to Equation (27) and CPO results in Figure 4).

In Scenario 2 (squares), the minimum time and minimum energy loss frontiers are equivalent to each other only for low inertia bump levels ρ_{ibR} (i.e., large inertia phase durations t_i), for which the condition (29) is satisfied. Otherwise, the frontiers bound a 3D Pareto frontier section, which is in agreement with the CPO results observed in Figure 4 and the algebraic analysis results given in Section 4. Note that the 3D frontier lower border corresponds to the inertia bump level $\rho_{ib,l} = 0.58$ established in Section 4.

In Scenario 4 (circles in Figure 9) the minimum time and minimum energy loss Pareto frontiers do not coincide with each other at any inertia bump level, thus forming a fully 3D overall Pareto frontier. This is because, in this scenario (and the full engine torque reduction case), the condition (29) is never satisfied, as discussed in Section 4. As a further confirmation of concurring CPO and simplified optimization results, it is worth noting that in the open torque converter case (Figure 9a) the control performance is better [i.e., the frontiers are closer to the utopia point (0, 0, 0)] than in the locked torque converter case (Figure 9b; cf. Figure 4). When compared to the CPO approach, the static optimization approach reduces the computational time from approximately 1 h for 6000 genetic algorithm evaluations to approximately 2 min.

The optimized shift control inputs are shown in Figure 9c,d. The ONC clutch torque generally grows with the increase of inertia bump level, i.e., decrease of inertia phase duration. This confirms the observations related to Equation (25). For the minimum time frontier, the OFG clutch torque is saturated at the maximum value (70 Nm herein, Table 3) and the ONC clutch torque levels are high. Hence, the clutches fight each other, and a negative power recirculation occurs via the OFG clutch [20]. The minimum energy loss

frontier is obtained by lowering the OFG clutch torque to its low-limit value (20 Nm), i.e., by minimizing the power recirculation. Note that there is an exception to this finding, which is related to Scenario 2 and where, in the region of satisfied condition (29) (i.e., for low inertia bump level), the minimum energy loss and minimum time frontiers are coincident with each other and obtained by using the maximum OFG clutch torque needed to achieve short shift time.

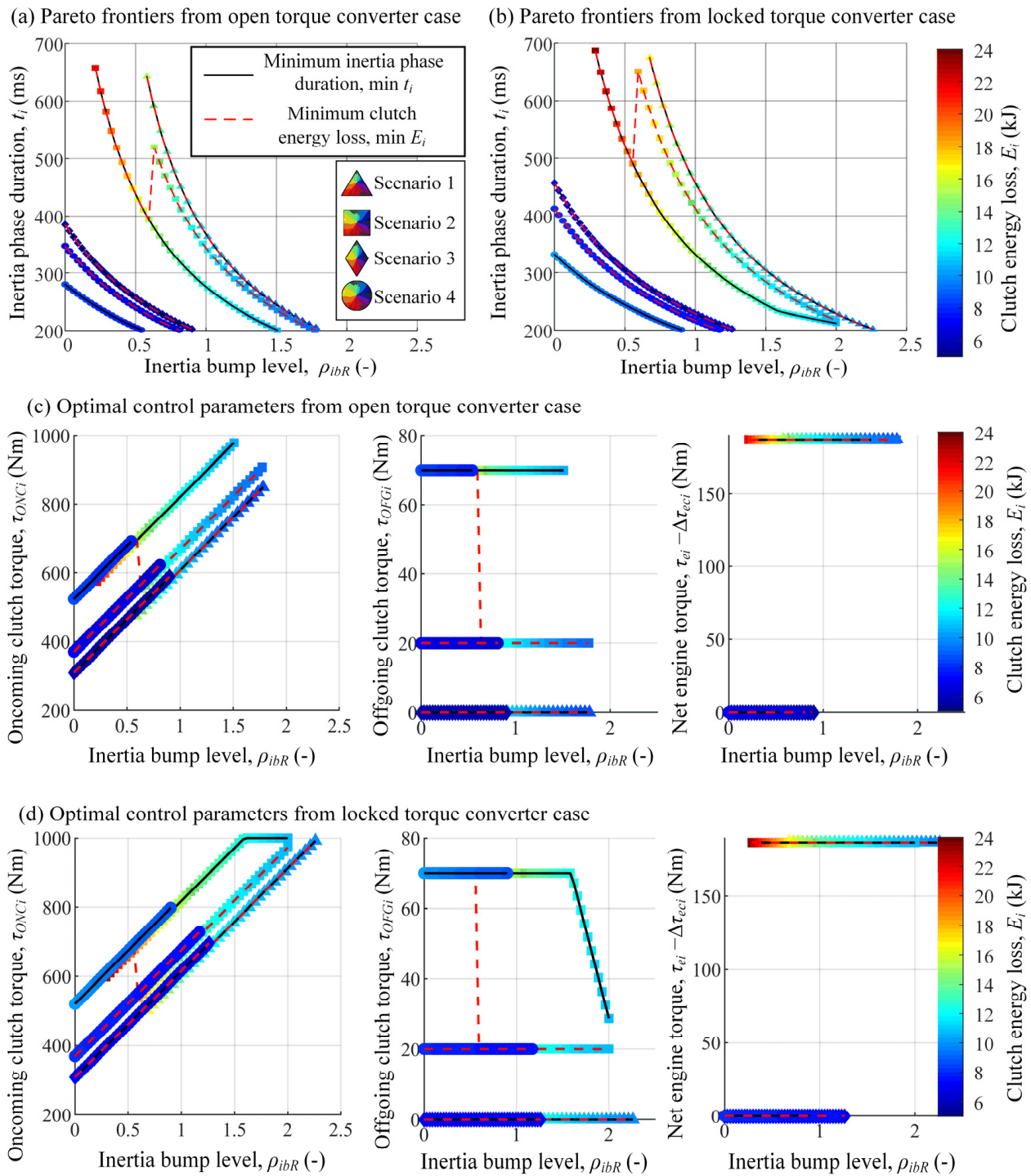


Figure 9. Static model-based optimization results for the inertia phase and constant control inputs, and cases of locked (a) and open torque converter (b) and corresponding optimal control parameters (c,d).

The engine torque reduction action, applied in Scenarios 3 and 4, is fully utilized in both the minimum time and minimum energy loss cases (net engine torque $\tau_{ei} - \Delta\tau_{eci}$ is zero), which confirms the analytical finding from Section 4 that reducing the engine torque is beneficial for reducing both shift time and energy loss.

5.1.2. Piecewise Linear Profile of Off-Going Clutch Torque Control Input

In the case of a piecewise linear OFG clutch torque profile (Figure 8), optimization has been conducted for the nominal, open torque converter case and 1–3 upshift. The control parameter constraints are given in Table 4, and they are again based on the control parameter ranges observed in the CPO results. A linear OFG clutch torque profile is also considered as a special case of the piecewise profile in Figure 8, which is obtained by setting $t_1 = t_2$ and $\tau_{OFG1} = 0$.

Table 4. Control parameter constraints for case of piecewise linear OFG clutch torque profile.

Constraints		
0 Nm	$\leq \tau_{ONCi} \leq$	1000 Nm
20 Nm	$\leq \tau_{OFG0} \leq$	70 Nm
10 Nm	$\leq \tau_{OFG1} \leq$	35 Nm
0 Nm	$\leq \Delta\tau_{eci} \leq$	τ_{ei}
50 ms	$\leq t_1 \leq$	0.4ti
100 ms	$\leq t_2 \leq$	0.8ti
	$t_1 \leq t_2$	

Figure 10 shows the Pareto frontiers corresponding to Scenarios 3 and 4. The lowest energy loss and slowest shift frontier corresponds to Scenario 3, where the OFG clutch torque is forced to zero. On the other hand, the fastest shift is represented by the minimum time frontier of Scenario 4, related to constant OFG clutch torque profile (circles). Applying the linear (squares) and piecewise linear profiles of OFG clutch torque (triangles) results in lower energy loss but a slower shift when compared to the constant OFG clutch torque profile. The shift is still faster than in Scenario 3, with comparable levels of energy loss, which confirms the effectiveness of using optimally controlled OFG clutch.

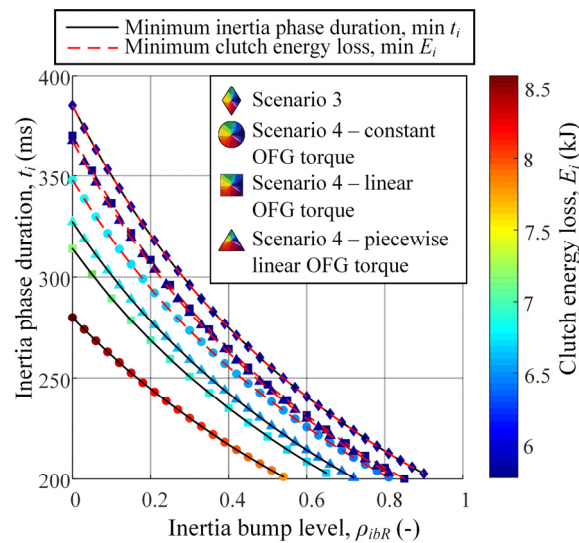


Figure 10. Static model-based optimization results for inertia phase, open torque converter case, Scenarios 3 and 4, and different types of OFG clutch torque profiles.

5.2. Simulation-Based Performance Analysis

The inertia phase control parameters obtained using static model-based parameter optimization (S-CPO) were applied within simulations of the nonlinear powertrain dynamics

model from Section 2 in order to calculate values of the objectives (5) considered in CPO for the overall shift (not only the inertia phase). This provides a direct comparison between the CPO and S-CPO results. Note that the S-CPO torque phase control profiles were adopted from the corresponding CPO results. The S-MPC ONC clutch torque discontinuity at the transition from the torque phase to the inertia phase was smoothed out by applying the torque rate limit used in the torque phase CPO formulation (Figure 3).

Figure 11 compares the CPO results (squares) and S-CPO results related to the minimum time (circles) and minimum energy loss boundary frontiers (diamonds), which were obtained for different profiles of control inputs, the open torque converter case, and a full-control scenario (Scenario 4). These plots indicate that the results of numerically efficient S-CPO approach the CPO benchmark results. Generally, using the constant OFG clutch torque profile (blue-edged circles) gives the lowest RMS jerk at the expense of the highest energy loss. This is due to the stronger activity of the constant OFG clutch torque profile in S-CPO compared to the piecewise linear profile in CPO. On the other hand, applying the linear and piecewise linear control profiles (red- and black-edged circles, respectively) results in a better-balanced overall S-CPO performance, which is in good agreement with the CPO benchmark performance.

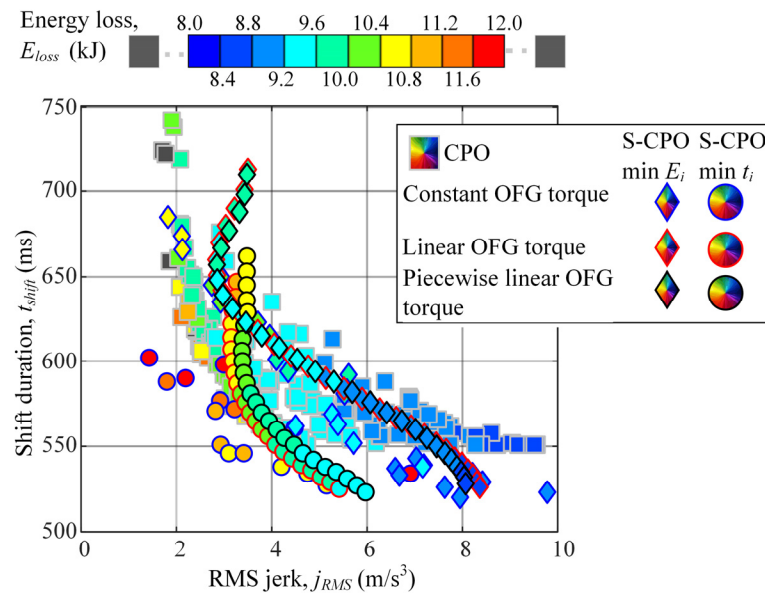


Figure 11. Comparative S-CPO and CPO results for Scenario 4, different types of control input profiles, and the case of an open torque converter.

6. Static Model-Based Predictive Control

The optimization results presented in the previous section have shown that it is possible to obtain control performance close to the CPO benchmark by relying on simple, static model-described objectives. In this section, the static model is used for derivation of an on-line ONC clutch predictive control law (S-MPC). The engine and OFG clutch torque represent the auxiliary open-loop control inputs, which can be profiled based on CPO or S-CPO results and which are anticipated by the model predictive controller.

6.1. Control System Design

6.1.1. Basic Control Law

Figure 12 illustrates the proposed static model-based predictive control (S-MPC). The control law derivation is based on the assumption that at a given time instance k during the inertia phase, a constant ONC clutch torque control is applied all over the prediction horizon that corresponds to the remaining inertia phase duration. That is, the prediction horizon includes the instants $k, k + 1, \dots, N_f$, where $N_f = t_i/T_s$ represents the length of the

inertia phase expressed in terms of the number of sampling steps, where the sampling time is denoted by T_s . Note that as the time progresses, the prediction horizon becomes narrower and diminishes at the end of inertia phase.

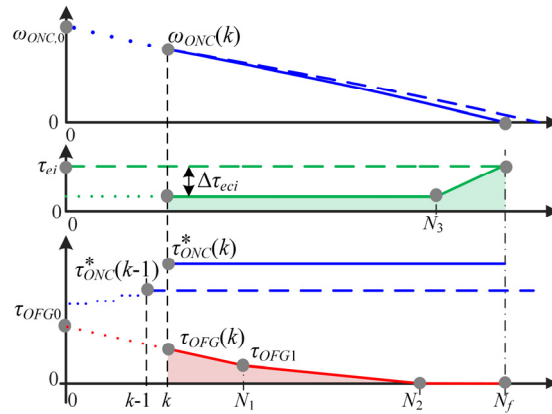


Figure 12. Illustration of static model-based predictive control (S-MPC).

The constant ONC clutch torque magnitude $\tau_{ONC}^*(k)$, required to complete the inertia phase at the desired end time t_i , is determined by assuming a linear fall of ONC clutch slip speed from its measured value at the step k , $\omega_{ONC}(k)$, towards zero at the final step N_f (Figure 12). The linear shape of ONC clutch slip speed is motivated by the CPO results shown in Figure 5 and discussed in Section 3. The control law for $\tau_{ONC}^*(k)$ anticipates a priori knowledge, i.e., open-loop determined engine and OFG clutch control input profiles over the prediction horizon, $\tau_e(t)$ and $\tau_{OFG}(t)$, respectively. Repeating the calculation process in all of the subsequent sampling steps and applying the determined control input $\tau_{ONC}^*(k)$ at the current sampling step results in an MPC-like feedback control action, which continuously corrects the ONC clutch torque command during the shift in order to satisfy the required inertia phase duration t_i .

Herein, the piecewise linear open-loop command of the engine torque, shown in Figure 12, is determined by a constant torque reduction $\Delta\tau_{eci}$, which linearly ceases towards the end of the inertia phase, starting from the step N_3 (cf. CPO profiles in Figure 3). The piecewise linear profile of the OFG clutch torque, shown in Figure 12, is based on the profile given in Figure 8, and it is defined by the parameters τ_{OFG0} , τ_{OFG1} , N_1 , and N_2 .

For the assumed linear ONC clutch slip speed profile and a constant output shaft speed ω_{os} [see Equation (6)], the input shaft speed profile is linear, as well. That is, the input shaft acceleration is constant, and it can be obtained by taking the time derivative of Equation (3b):

$$\dot{\omega}_{is,i}(k) = -\frac{\omega_{ONC}(k)}{i_2(N_f - k)T_s}, \tag{30}$$

The constant ONC clutch torque command $\tau_{ONC}^*(k)$ is obtained by integrating Equation (9a) over the prediction horizon $[kT_s, N_fT_s]$ and accounting for Equation (30) (see the control law block diagram shown in Figure 13):

$$\tau_{ONC}^* = \frac{1}{i_2} \left(\underbrace{\frac{R_\tau \int_{kT_s}^{N_fT_s} \tau_e(t) dt}{(N_f - k)T_s}}_{\tau_{e,p}(k)} - \underbrace{\frac{i_1 \int_{kT_s}^{N_fT_s} \tau_{OFG}(t) dt}{(N_f - k)T_s}}_{\tau_{OFG,p}(k)} + \frac{I_{eq}}{i_2(N_f - k)T_s} \omega_{ONC}(k) \right) \tag{31}$$

where the first and second right-hand side terms correspond to the engine torque mean value anticipation $\tau_{e,p}$ and the OFG clutch torque mean value anticipation $\tau_{OFG,p}$, respec-

tively. For the open-loop torque profiles defined in Figure 12, the final solutions for these two terms read:

$$\tau_{e,p}(k) = \begin{cases} R_\tau \left(\tau_{ei} + \Delta\tau_{eci} \frac{2k-N_f-N_3}{2(N_f-k)} \right), & \text{for } k \leq N_3 \\ R_\tau \left(\tau_{ei} - \frac{\Delta\tau_{eci}}{2} \frac{N_f-k}{N_f-N_3} \right), & \text{otherwise} \end{cases} \quad (32)$$

$$\tau_{OFG,p}(k) = \begin{cases} \frac{i_1}{2} \tau_{OFG0} \frac{(N_1-k)^2}{N_1(N_f-k)} + \frac{i_1}{2} \tau_{OFG1} \frac{N_1 N_2 - k^2}{N_1(N_f-k)}, & \text{for } k \leq N_1 \\ \frac{i_1}{2} \tau_{OFG1} \frac{(N_2-k)^2}{(N_2-N_1)(N_f-k)}, & \text{for } N_1 < k \leq N_2 \\ 0, & \text{otherwise} \end{cases} \quad (33)$$

Note that for the last prediction step ($k = N_f$), the difference term $N_f - k$, which is present in denominators of Equation (31) is set to 1 (rather than zero) in order to avoid the equation singularity.

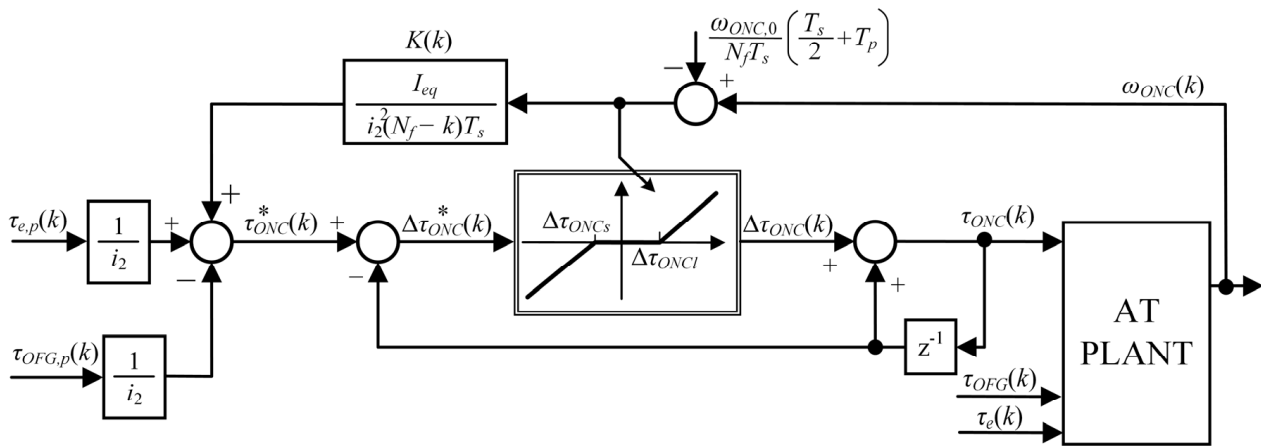


Figure 13. Block diagram of S-MPC law, including control signal difference dead zone.

In order to account for the delay due to sampling and the ZOH process ($T_s/2$, [29]) as well as possible actuation delays (T_p), the ONC clutch slip speed correction (ω_{ONC}^*) should be used in Equation (31) instead of the measured one (ω_{ONC}). The corrected signal is again obtained by assuming the linearly falling slip speed [cf. Equation (30) and see Figure 13]:

$$\omega_{ONC}^*(k) = \omega_{ONC}(k) - \frac{\omega_{ONC,0}}{N_{max} T_s} \left(\frac{T_s}{2} + T_p \right), \quad (34)$$

where $\omega_{ONC,0}$ is the ONC clutch slip speed sampled at the start of inertia phase.

6.1.2. Control Signal Difference Dead Zone

The ONC slip speed feedback control gain term $K(k)$, designated in Figure 13, evidently increases as the prediction horizon diminishes (i.e., when k approaches N_f). This can cause the effect of relative or even absolute instability of the control system near the end of the inertia phase. Furthermore, in an early stage of the inertia phase, the discrete-time closed-loop control system pole can assume large negative real values for realistic sampling time values (e.g., 10 ms), thus causing high-frequency oscillation known as the ringing effect [29]. These effects are illustrated in Appendix B by a root-locus analysis.

In order to suppress instability and ringing effects, the control command $\tau_{ONC}^*(k)$ given by Equation (31) is modified by applying the control signal difference dead zone element, as shown in Figure 13. The dead zone element blocks the control command $\tau_{ONC}^*(k)$ and applies the previous command $\tau_{ONC}(k-1)$ if the difference $\tau_{ONC}^*(k) - \tau_{ONC}(k-1)$ is within the dead zone threshold $\Delta\tau_{ONCs,l}$ (Figure 13). In this way the controller gain is

temporarily reduced to zero, which provides a stabilizing effect at the expense of introducing an allowable deviation from the target inertia phase duration $t_i = N_f T_s$. The dead zone threshold is determined as the difference between the exact/original command and the one related to the maximum allowable deviation of the inertia phase duration. Based on Equation (31), one obtains the following expression for time-varying dead zone threshold:

$$\Delta\tau_{ONCs,l}(k) = \left(\frac{1}{(N_f - k)T_s} - \frac{1}{\lambda_{s,l}(N_f - k)T_s} \right) \frac{I_{eq}}{i_2^2} \omega_{ONC}^*(k), \quad (35)$$

where $\lambda_l > 1$ and $\lambda_s < 1$ represent the tunable factors that determine the allowed lower and upper inertia phase duration deviation, respectively. They are tuned to $\lambda_l = 1.1$ and $\lambda_s = 0.9$ herein as a good trade-off between the chattering suppression efficiency and allowable inertia phase duration control error (+/−10%).

6.2. Simulation Verification Results

The S-MPC strategy is implemented within the nonlinear powertrain simulation model and compared with the CPO benchmark results for the full-control scenario (Scenario 4), open torque converter case, and 1–3 upshift. The open-loop control profiles of the engine and OFG clutch torque, as well as the torque phase control inputs, were adopted from the corresponding CPO results. The S-MPC law target inertia phase duration was equated with the one corresponding to the CPO solution. The sampling time was set to $T_s = 10$ ms.

The performance plot shown in Figure 14 indicates that the Pareto frontier obtained by the on-line S-MPC strategy (circles) is comparable with the off-line CPO benchmark (squares). The S-MPC strategy even reduces the RMS jerk and energy loss for fast shifts to some extent, which is due to its ability to freely shape the ONC clutch torque, as opposed to piecewise linear CPO profiles. This is illustrated by the comparative time responses given in Figure 15 for the S-MPC and CPO designs designated by red and magenta circles in Figure 14, as well as the corresponding performance indices listed in Table 5.

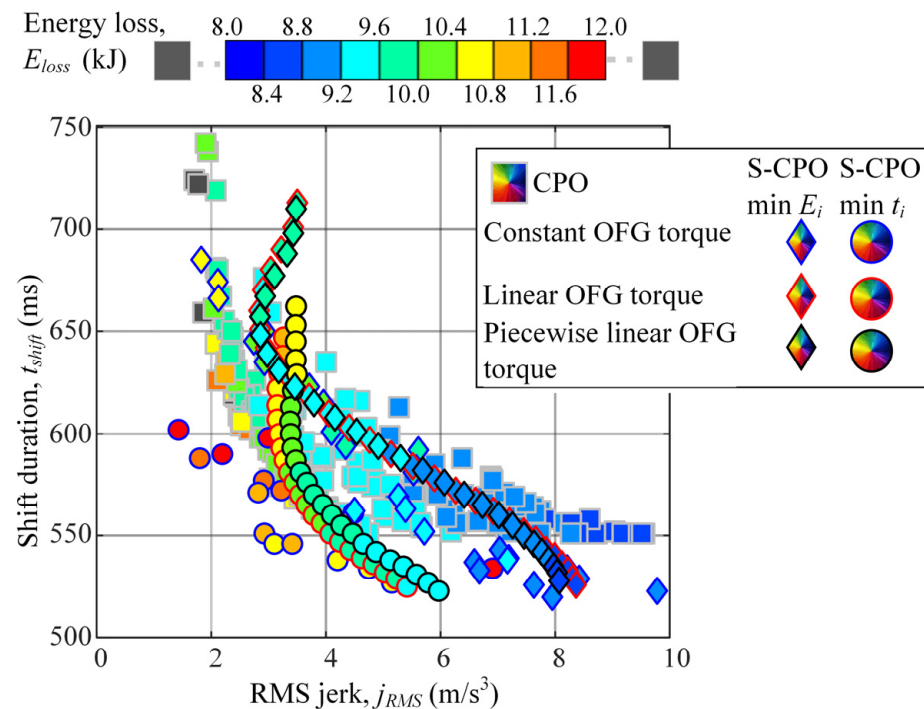


Figure 14. Comparative performance plots of S-MPC and CPO.

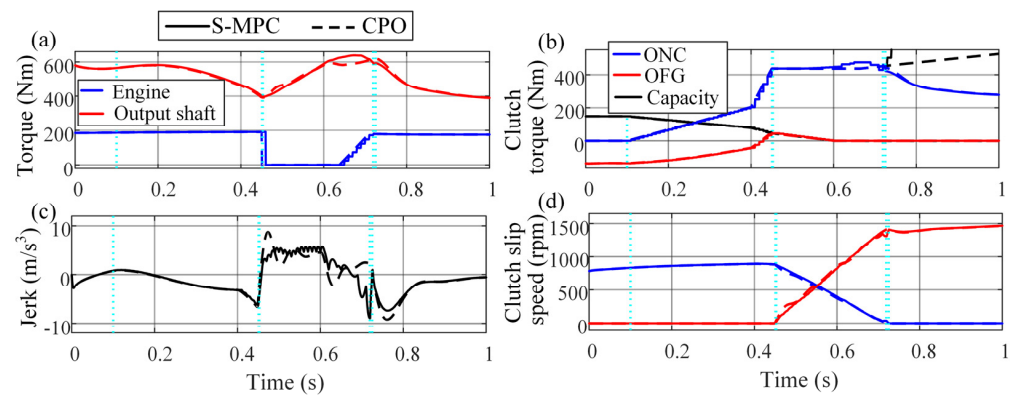


Figure 15. Comparative S-MPC and CPO time responses corresponding to designs designated in Figure 14.

Table 5. Comparative S-MPC and CPO performance indices corresponding to designs designated in Figure 14.

	t_{shift} (ms)	t_i (ms)	E_{loss} (kJ)	j_{RMS} (m/s ³)
CPO	619	268	9.76	2.69
S-MPC	625 (+1%)	272 (+1.5%)	9.85 (+1%)	2.62 (−3%)

Figure 16 illustrates the effect of introducing the dead zone element in the S-MPC strategy in Figure 13. In the absence of a dead zone element, the ONC clutch torque command exhibits certain ringing at the start of the inertia phase and chattering/instability towards the end of inertia phase (Figure 16b). This is manifested in increased jerk peaks at the start and end of the inertia phase (Figure 16d), and also in closing the ONC clutch too early (Figure 16c). When applying the dead zone element, the overall response is dampened since the dead zone element intermittently sets the feedback gain K to zero (Figure 16e).

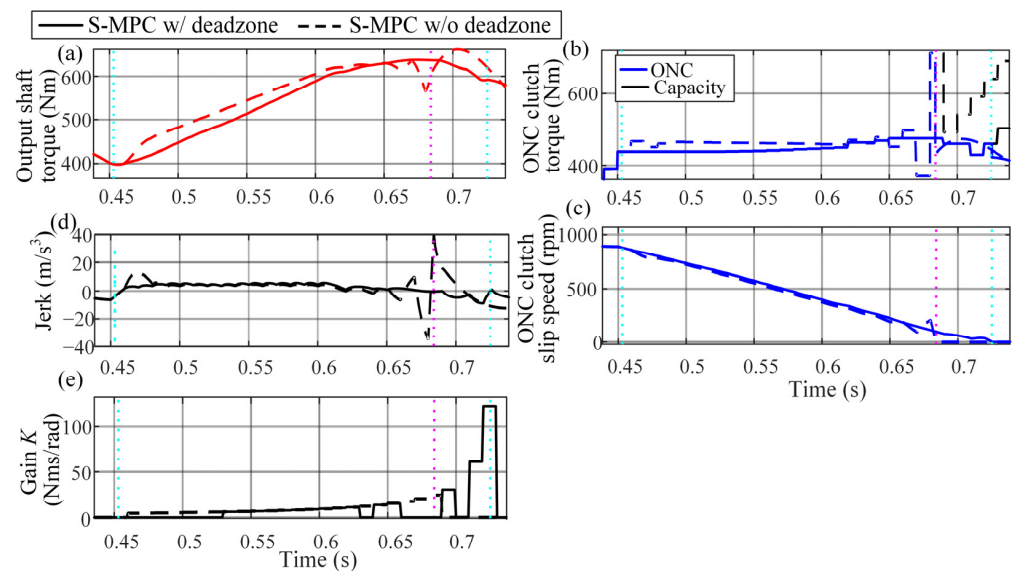


Figure 16. Inertia phase time responses of output shaft torque (a), ONC clutch torque (b) and speed (c), jerk (d) and feedback gain (e) for S-MPC strategies with and without dead zone element incorporated.

Another key feature of the S-MPC strategy is that it incorporates the feedback path through the ω_{ONC} signal (Figure 13), which makes it robust with respect to disturbances (including parameter variations). This is illustrated by the comparative S-MPC vs. CPO performance indices given in Table 6 for the case of perturbing the lumped impeller and

engine inertia I_{ei} in the simulation (AT) model, within the range of $\pm 20\%$ from the nominal value used in the S-MPC and CPO control strategies. By adjusting the ONC clutch torque through feedback actions, the S-MPC strategy provides accurate inertia phase duration t_i for the perturbed AT model, while the open-loop CPO control is sensitive to AT parameter variations. Also, the RMS jerk and energy loss indices are closer to the nominal case in the great majority of analyzed cases.

Table 6. Performance metrics of S-MPC and CPO systems for different ratios of actual and nominal engine + impeller inertia.

$I_{ei}/I_{ei,nom}$	t_{shift} (ms)	CPO			S-MPC			
		t_i (ms)	E_{loss} (kJ)	j_{RMS} (m/s ³)	t_{shift} (ms)	t_i (ms)	E_{loss} (kJ)	j_{RMS} (m/s ³)
0.8	576 (−7%)	223 (−17%)	9.1 (−6%)	3.34 (+24%)	621 (−1%)	266 (−2%)	9.4 (−5%)	2.59 (−1%)
0.9	595 (−4%)	243 (−9%)	9.4 (−3%)	2.83 (+5%)	619 (−1%)	265 (−3%)	9.6 (−2%)	2.50 (−4%)
1.0	619 (0%)	268 (0%)	9.8 (0%)	2.69 (0%)	625 (0%)	272 (0%)	9.9 (0%)	2.62 (0%)
1	650 (+5%)	299 (+12%)	10.1 (+3%)	2.68 (0%)	619 (−1%)	267 (−2%)	10.0 (+2%)	2.94 (+12%)
1.1	680 (+10%)	330 (+23%)	10.4 (+7%)	2.75 (+2%)	627 (0%)	275 (+1%)	10.2 (+3%)	3.11 (+19%)
1.2	576 (−7%)	223 (−17%)	9.1 (−6%)	3.34 (+24%)	621 (−1%)	266 (−2%)	9.4 (−5%)	2.59 (−1%)

Similarly, the S-MPC system has been found to be robust with respect to unmodeled actuator dynamics. This is illustrated in Figure 17, where the ‘w/actuator dynamics’ case concerns the use of a pure delay + lag clutch actuator model with the lag time constant of 30 ms and the pure delay of 10 ms, where only the latter is partly accounted for in the control strategy through the correction (34). The actuator dynamics delay the clutch torque capacities, which naturally causes a prolonged response in the open-loop-controlled torque phase. However, the S-MPC strategy maintains the inertia phase duration close to the target value due to its feedback control ability, and at the same time preserves a high level of stability.

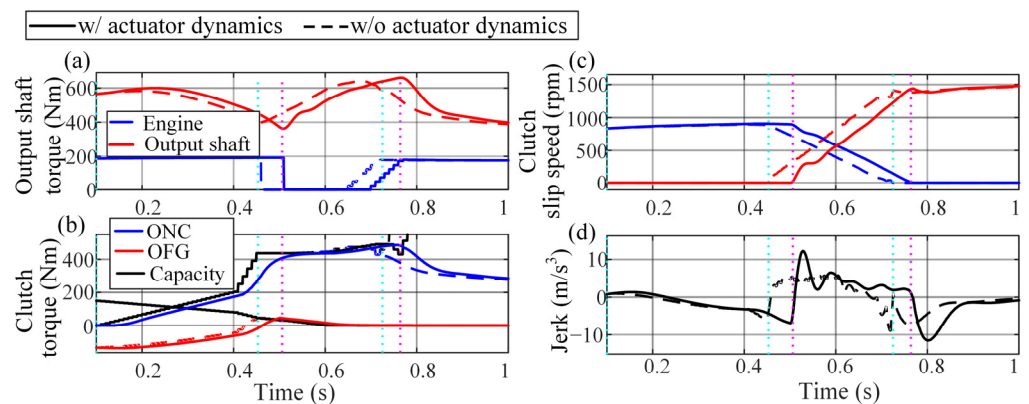


Figure 17. Time responses of torques (a), ONC clutch torque (b) and speed (c), and jerk (d) for S-MPC strategies with and without clutch actuator dynamics included in AT model.

7. Conclusions

Replacing the powertrain dynamics model and related optimization objectives with simplified, static expressions for inertia phase duration, energy loss, and inertia bump ob-

jectives, as functions of control input profile parameters, facilitates control parameter optimization and control performance algebraic analyses. The objective expressions have been obtained for two characteristic control scenarios: (i) constant control inputs that includes oncoming (ONC) and off-going (OFG) clutch torque, and engine torque reduction; and (ii) a piecewise linear profile of OFG clutch torque, while keeping the ONC clutch and engine torque reduction constant.

Algebraic analysis was conducted based on the assumptions of constant output shaft speed, linear ONC clutch slip speed profile, constant control inputs, and locked torque converter. The analysis has shown that the inertia phase duration can be reduced by boosting the engine torque reduction, increasing the OFG clutch torque, and raising the allowable level of inertia bump. When applying the OFG clutch control input, there is an inertia bump level above which the clutch energy loss increases with shortening of the shift, thus switching the Pareto frontier from 2D to 3D shape (all the three objectives become conflicting). The above observations have been illustrated by static objective model-based numerical optimization results. They both agree with the genetic algorithm-based control parameter optimization (CPO) benchmark results, which showed that by using the OFG clutch control, the inertia phase duration could be reduced by 20% at the expense of clutch energy loss rise of 4%.

The insights gained by applying the simplified off-line optimization approach have been employed for the derivation of an on-line static model-based predictive control (S-MPC) strategy. The S-MPC strategy commands the oncoming clutch torque capacity on the shrinking, inertia phase horizon based on two actions: (i) an oncoming clutch slip-speed feedback term designed to achieve the target inertia phase duration, and (ii) anticipation of open-loop mean-value control actions of engine torque reduction and off-going clutch torque. The oncoming clutch torque capacity command is further modified by a control signal difference dead zone element in order to suppress chattering effects. The simulation verification results have indicated that the S-MPC strategy can provide performance comparable to the CPO benchmark. For certain faster shift designs, S-MPC outperforms CPO in terms of reduced RMS jerk, owing to its ability to freely shape the ONC clutch torque profile, as opposed to the piecewise linear open-loop profile used in CPO. A robustness analysis has shown that in the case of AT parameter variations the S-MPC system maintains the control performance (in particular the shift time) close to that of the nominal system, i.e., within $\pm 1\%$ compared to $\pm 10\%$ in the CPO case. This is because of the inherent ONC clutch slip speed feedback loop incorporated in the S-MPC law. Similarly, the S-MPC system is rather insensitive to unmodeled clutch actuator dynamics.

The main advantage of the proposed control strategy lies in its ability to provide MPC functionality while being simple and practical to implement and tune. Since the S-MPC strategy relies upon the existing ONC clutch slip speed feedback in order to determine the ONC clutch torque demand, it can readily substitute the existing closed-loop controllers. From the tuning perspective, the calibration engineer only needs to set the desired shift duration, while the time-varying feedback gain is automatically determined by the strategy. However, the strategy still relies on calibration or off-line-optimization of the open-loop OFG clutch torque demand and engine control input, and as such, it is strictly speaking sub-optimal. Therefore, the future work will mainly be directed towards the development of more general, on-line-implementable, multi-input MPC strategies. They would be aimed at reproducing the CPO benchmark performance while incorporating inherent feedback paths through all control channels. The herein presented and future MPC strategies are aimed to be extended to torque phase control, as well.

Author Contributions: Conceptualization, I.C., M.H., J.D., Y.Z., V.I. and Y.F.; methodology, I.C., M.H., Y.Z. and J.D.; software, I.C. and M.H.; formal analysis, I.C. and J.D.; writing—original draft preparation, I.C. and M.H.; writing—review and editing, J.D., V.I. and Y.F.; visualization, I.C. and M.H.; supervision, J.D., Y.Z., V.I. and Y.F.; project administration, J.D. and Y.Z.; funding acquisition, J.D. and Y.F. All authors have read and agreed to the published version of the manuscript.

Funding: This research was funded by the Ford Motor Company.

Data Availability Statement: Not applicable.

Acknowledgments: It is gratefully acknowledged that the research work of the first author was supported by the Croatian Science Foundation through the “Young researchers’ career development project—training of new doctoral students”.

Conflicts of Interest: The authors declare no conflict of interest.

Nomenclature

Symbols		Subscripts	
I	Inertia	e	Engine
i	AT input shaft-clutch torque ratio	is	Input shaft
g	Clutch-AT output shaft torque ratio	io	Input-to-output shaft
E_{loss}	Dissipated energy in clutches	os	Output shaft
j_{RMS}	Root mean square of vehicle jerk	ONC	Oncoming (clutch)
t	Time	OFG	Off-going (clutch)
t_{shift}	Shift time	1	Off-going clutch path
ω	Speed	2	On-coming clutch path
τ	Torque		
γ	Gear ratio		

Abbreviations

Abbreviation	Meaning
AT	Automatic transmission
CPO	Control parameter optimization
CTO	Control trajectory optimization
OFG	Off-going clutch
ONC	Oncoming clutch
RMS	Root mean square
S-CPO	Static model-based control parameter optimization
S-MPC	Static model-based predictive control
SQP	Sequential quadratic program

Appendix A. Clutch Energy Loss for Piecewise Linear Shape of Off-Going Clutch Torque

Solving Equation (14) for the control input profiles from Figure 8, which are characterized by the piecewise linear shape of the OFG clutch torque, gives the following final equation for the total clutch energy loss:

$$\begin{aligned}
 E_i = & \frac{i_1 k_{1OFG} t_1^2}{8} (\tau_{OFG0}^2 + \tau_{OFG1}^2) \\
 & + \tau_{ONCi} t_i \omega_{osi} \left(\frac{t_2}{i_1 g_1} - \frac{1}{g_2} \right) + \frac{\tau_{ONCi} i_2 k_{1ONC} t_i^2}{2} \\
 & + \tau_{OFG1}^2 i_1 k_{1OFG} \left(\frac{t_1^3 + t_1 t_2^2}{4 \Delta t_2} + \frac{t_1^4 + t_2^4}{8 \Delta t_2^2} + \frac{3 t_1^2 t_2^2}{4 \Delta t_2^2} - \frac{t_1^2 t_2}{2 \Delta t_2} - \frac{t_1 t_2^3 + t_1^3 t_2}{2 \Delta t_2^2} \right) \\
 & + \frac{\tau_{eo} \tau_{OFG0} i_1 k_{1e} t_1^2}{6} + \frac{\tau_{eo} \tau_{ONCi} i_2 k_{1e} t_i^2}{2} \\
 & + \tau_{eo} \tau_{OFG1} i_1 k_{1e} \left(\frac{t_1^2}{3} + \frac{t_1^3}{3 \Delta t_2} + \frac{t_2^3}{6 \Delta t_2} - \frac{t_1^2 t_2}{2 \Delta t_2} \right) \\
 & + \tau_{OFG0} \tau_{OFG1} i_1 k_{1OFG} \left(\frac{t_1^2}{4} + \frac{t_1^3 + t_1 t_2^2}{4 \Delta t_2} - \frac{t_1^2 t_2}{2 \Delta t_2} \right) \\
 & + \tau_{OFG0} \tau_{ONCi} \left(\frac{i_1 k_{1ONC} t_1^2}{6} + \frac{i_2 k_{1OFG} t_1 t_i}{2} - \frac{i_2 k_{1OFG} t_1^2}{6} \right) \\
 & + \tau_{OFG1} \tau_{ONCi} i_1 k_{1ONC} \left(\frac{t_1^2}{3} + \frac{t_1^3}{3 \Delta t_2} + \frac{t_2^3}{6 \Delta t_2} - \frac{t_1^2 t_2}{2 \Delta t_2} \right) \\
 & + \tau_{OFG1} \tau_{ONCi} i_2 k_{1OFG} \left(\frac{3 t_1 t_i - 2 t_1^2}{6} - \frac{2 t_1^3 + t_2^3}{6 \Delta t_2} + \frac{t_1^2 t_2 + t_1^2 t_i + t_2^2 t_i - 2 t_1 t_2 t_i}{2 \Delta t_2} \right)
 \end{aligned} \tag{A1}$$

where t_i is given by Equation (21), I_{eq} is defined by Equation (10a), and the following substitutions apply:

$$\begin{aligned}
 k_{1ONC} &= \frac{-i_2}{I_{eq}} \\
 k_{1OFG} &= \frac{-i_1}{I_{eq}} \\
 k_{1e} &= \frac{R_r}{I_{eq}} \\
 \Delta t_2 &= t_2 - t_1 \\
 \tau_{e0} &= \tau_{ei} - \Delta \tau_{eci}
 \end{aligned}
 \tag{A2}$$

Appendix B. Root-Locus Analysis of Ringing and Instability Effects

The root-locus analysis is based on the transfer function of closed-loop system containing the S-MPC law given by Equation (31). First, the clutch actuator and driveline dynamic are neglected, and the torque converter is assumed to be locked. Under those assumptions, the following discrete-time AT transfer function is obtained from Equation (3):

$$G_{ONC}(z) = \frac{\omega_{ONC}(z)}{\tau_{ONC}(z)} = \frac{\mathbf{L}_{red}(2,4)T_s}{z-1},
 \tag{A3}$$

where $\mathbf{L}_{red} = \mathbf{U}_{red}\mathbf{A}_{red}^{-1}\mathbf{B}_{red}$. Combining the feedback component of S-MPC control law (31) with Equation (A3) gives the closed-loop characteristic polynomial:

$$N(z) = \text{Num}(1 + G_o(z)) = z - 1 - \mathbf{L}_{red}(2,4)KT_s
 \tag{A4}$$

where $G_o(z) = -KG_{ONC}(z)$, and K is a time-varying feedback controller gain defined in Figure 13.

Figure A1a shows the root-locus plot related to characteristic polynomial (A4) and sampling time $T_s = 10$ ms. The closed-loop system pole moves to the left and exits the well-damped area ($\zeta = 0.71$) as the remaining inertia phase duration $N_f - k$ reduces, i.e., as the feedback gain $K(k)$ grows. This causes the ringing tendency in the early stage of inertia phase. In the final stage of inertia phase, the closed-loop pole eventually exits the stability region (the unit circle), and the system becomes unstable.

Figure A1b shows the root-locus plot for the case of the full AT model, locked torque converter, and the actuator dynamics described by pure delay of 10 ms and lag term with the time constant of 30 ms. In addition to the ringing effect-related pole (which are now more suppressed, cf. Figure A1a), there is a pair of additional conjugate-complex poles that exit the unit circle as the inertia phase progresses, i.e., $K(k)$ increases. These poles explain the instability effect.

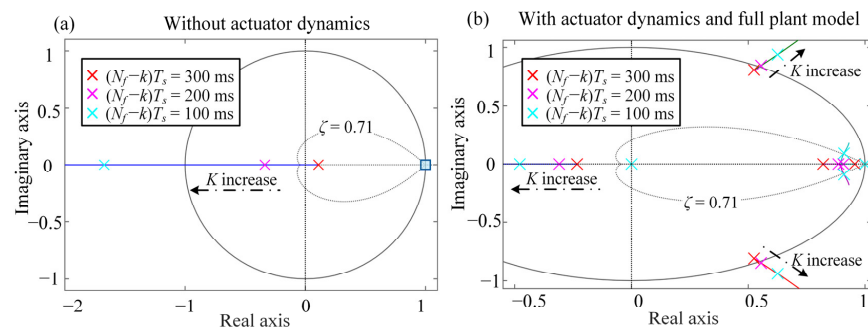


Figure A1. Root-locus plots of closed-loop discrete-time system for simplified AT model (a) and full AT model including actuator dynamics (b) ($N_f = 30$ and $T_s = 10$ ms; locked torque converter is considered in both cases).

References

- Bai, S.; Maguire, J.; Peng, H. *Dynamic Analysis and Control System Design of Automatic Transmissions*; SAE International: Warrendale, PA, USA, 2013. [CrossRef]
- Greiner, J.; Grumbach, M. Automatic Transmission Systems Beyond 2020- Challenger and Competition. SAE Tech. Paper; 2013; p. 2013-01-1273. [CrossRef]

3. Li, D. Control and Integration Challenges for Future Automatic Transmissions. *SAE Int. J. Engines* **2016**, *9*, 1881–1890. [[CrossRef](#)]
4. Wurm, M.S.A.; Bestle, D. New Approach for Transmission Calibration—Model-based Multi-Objective Optimization Via SIL. In Proceedings of the 7th International Symposium and Exhibition, Innovative Automotive Transmission, Hybrid & Electric Drives, Detroit, MI, USA, 13–15 May 2013.
5. Ranogajec, V.; Coric, M.; Deur, J.; Ivanovic, V. Multi-objective Parameter Optimization of Automatic Transmission Shift Control Profiles. *SAE Tech. Paper* **2018**, 2018-01-1164. [[CrossRef](#)]
6. Ranogajec, V.; Deur, J.; Ivanović, V.; Tseng, H.E. Multi-objective parameter optimization of control profiles for automatic transmission double-transition shifts. *Control Eng. Pract.* **2019**, *93*, 104183. [[CrossRef](#)]
7. Zhang, H.; Zhao, X.; Yang, J.; Zhang, W. Optimizing Automatic Transmission Double-Transition Shift Process Based on Multi-Objective Genetic Algorithm. *Appl. Sci.* **2020**, *10*, 7794. [[CrossRef](#)]
8. Čorić, M.; Ranogajec, V.; Deur, J.; Ivanović, V.; Tseng, H.E. Optimization of Shift Control Trajectories for Step Gear Automatic Transmissions. *J. Dyn. Syst. Meas. Control* **2017**, *139*, 061005. [[CrossRef](#)]
9. Ranogajec, V.; Ivanović, V.; Deur, J.; Tseng, H.E. Optimization-based assessment of automatic transmission double-transition shift controls. *Control Eng. Pract.* **2018**, *76*, 155–166. [[CrossRef](#)]
10. Gao, B.; Chen, H.; Sanada, K. Two-Degree-of-Freedom Controller Design for Clutch Slip Control of Automatic Transmission. *SAE Int. J. Passeng. Cars-Mech. Syst.* **2009**, *1*, 430–438. [[CrossRef](#)]
11. Mishra, K.D.; Srinivasan, K. Robust control and estimation of clutch-to-clutch shifts. *Control Eng. Pract.* **2017**, *65*, 100–114. [[CrossRef](#)]
12. Mishra, K.; Srinivasan, K. Improved Integrated Powertrain Control of Gearshifts Using Linear Parameter Varying Control. In Proceedings of the 2019 American Control Conference (ACC), Philadelphia, PA, USA, 10–12 July 2019; pp. 4553–4558. [[CrossRef](#)]
13. Liu, F.; Chen, L.; Li, D.; Yin, C. Improved Clutch Slip Control for Automated Transmissions. *Proc. Inst. Mech. Eng. Part C J. Mech. Eng. Sci.* **2018**, *232*, 3181–3199. [[CrossRef](#)]
14. Cvok, I.; Deur, J.; Ivanovic, V.; Zhang, Y.; Fujii, Y. An LQR Approach of Automatic Transmission Upshift Control Including Use of Off-going Clutch within Inertia Phase. *SAE Int. J. Adv. Curr. Pract. Mobil.* **2020**, *2*, 2081–2091. [[CrossRef](#)]
15. Soldo, J.; Cvok, I.; Deur, J.; Ivanovic, V.; Zhang, Y.; Fujii, Y. Automatic Transmission Upshift Control Using a Linearized Reduced-Order Model-Based LQR Approach. *SAE Int. J. Adv. Curr. Pract. Mobil.* **2021**, *3*, 2290–2300. [[CrossRef](#)]
16. Liu, Q.; Guo, L.; Gao, B.; Ye, K.; Chen, H.; Guo, H. Coordinate Receding Horizon Control for the Power-Shift Process of Multi-speed Electric Vehicles. *IEEE Trans. Veh. Technol.* **2019**, *69*, 1055–1059. [[CrossRef](#)]
17. Mesmer, F.; Szabo, T.; Graichen, K. Embedded Nonlinear Model Predictive Control of Dual-Clutch Transmissions with Multiple Groups on a Shrinking Horizon. *IEEE Trans. Control Syst. Technol.* **2018**, *27*, 2156–2168. [[CrossRef](#)]
18. Ranogajec, V.; Deur, J.; Coric, M. Bond Graph Analysis of Automatic Transmission Shifts including Potential of Extra Clutch Control. *SAE Int. J. Engines* **2016**, *9*, 1929–1945. [[CrossRef](#)]
19. Zhang, Y.; Haria, H.; Hippalgaonkar, R.; Pietron, G.; Fujii, Y. Automatic Transmission Shift Control for Canceling Inertia Torque. *SAE Tech. Paper* **2018**, 2018-01-1167. [[CrossRef](#)]
20. Cvok, I.; Ranogajec, V.; Deur, J.; Zhang, Y.; Ivanovic, V.; Fujii, Y. Analysis of Improving Automatic Transmission Upshift Performance by Using Off-Going Clutch during Inertia Phase. *J. Dyn. Syst. Meas. Control* **2021**, *144*, 021005. [[CrossRef](#)]
21. Hrovat, D.; Tobler, W. Bond Graph Modeling of Automotive Power Trains. *J. Frankl. Inst.* **1991**, *328*, 623–662. [[CrossRef](#)]
22. Deur, J.; Asgari, J.; Hrovat, D.; Kovač, P. Modeling and Analysis of Automatic Transmission Engagement Dynamics-Linear Case. *J. Dyn. Syst. Meas. Control* **2005**, *128*, 263–277. [[CrossRef](#)]
23. Goleski, G.D.; Baldwin, R.A. Multi-Speed Transmission. U.S. Patent 8,545,362 B1, 1 October 2013.
24. Ivanovic, V.; Tseng, H.E. Bond Graph Based Approach for Modeling of Automatic Transmission Dynamics. *SAE Int. J. Engines* **2017**, *10*, 1999–2014. [[CrossRef](#)]
25. Ranogajec, V.; Deur, J. An Automated Model-Order Reduction Method for Automatic Transmissions. *J. Dyn. Syst. Meas. Control* **2017**, *139*, 071004. [[CrossRef](#)]
26. Ranogajec, V.; Deur, J. Bond Graph Analysis of Automatic Transmission Double-Transition Shift Dynamics. In Proceedings of the International Conference on Bond Graph Modeling (ICBGM 2018), Bordeaux, France, 9–12 July 2018; p. 11.
27. Karnopp, D. Computer Simulation of Stick-Slip Friction in Mechanical Dynamic Systems. *J. Dyn. Syst. Meas. Control* **1985**, *107*, 100–103. [[CrossRef](#)]
28. Zhang, Y.; Fujii, Y.; Hippalgaonkar, R.; Cvok, I.; Ivanovic, V.; Deur, J.; Ranogajec, V. Mathematical Analysis of Clutch Thermal Energy during Automatic Shifting Coupled with Input Torque Truncation. *SAE Tech. Paper* **2020**, 2020-01-0967. [[CrossRef](#)]
29. Isermann, R. *Digital Control Systems*; Springer: Berlin/Heidelberg, Germany, 1989. [[CrossRef](#)]

Disclaimer/Publisher’s Note: The statements, opinions and data contained in all publications are solely those of the individual author(s) and contributor(s) and not of MDPI and/or the editor(s). MDPI and/or the editor(s) disclaim responsibility for any injury to people or property resulting from any ideas, methods, instructions or products referred to in the content.